

Redox Activity and Two-Step Valence Tautomerism in a Family of Dinuclear Cobalt Complexes with a Spiroconjugated Bis(dioxolene) Ligand

Kerwyn G. Alley,[†] Giordano Poneti,^{‡,§} Peter S. D. Robinson,[†] Ayman Nafady,^{⊥,∇} Boujemaa Moubaraki,[⊥] Jade B. Aitken,^{||} Simon C. Drew,[#] Chris Ritchie,[†] Brendan F. Abrahams,[†] Rosalie K. Hocking,[⊥] Keith S. Murray,[⊥] Alan M. Bond,[⊥] Hugh H. Harris,[○] Lorenzo Sorace,[‡] and Colette Boskovic^{*,†}

[†]School of Chemistry, and [#]Mental Health Research Institute, The University of Melbourne, Victoria, 3010, Australia

[‡]UdR INSTM and Department of Chemistry "U. Schiff", University of Florence, 50019 Sesto Fiorentino (FI), Italy

[§]Department of Applied Science and Technology, Guglielmo Marconi University, 00193, Rome, Italy

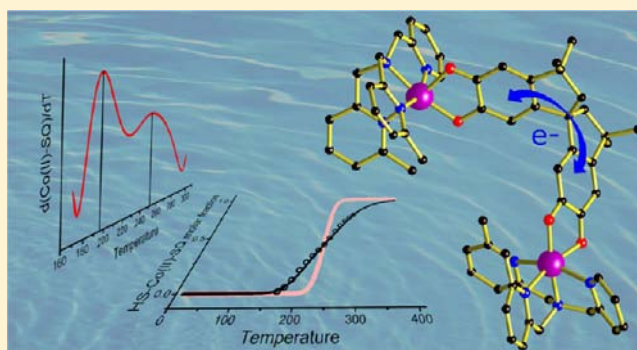
[⊥]School of Chemistry, Monash University, Clayton, Victoria, 3800, Australia

^{||}School of Chemistry, The University of Sydney, New South Wales, 2006, Australia

[○]School of Chemistry and Physics, The University of Adelaide, South Australia, 5005, Australia

Supporting Information

ABSTRACT: A family of dinuclear cobalt complexes with bridging bis(dioxolene) ligands derived from 3,3,3',3'-tetramethyl-1,1'-spirobis(indane-5,5',6,6'-tetrol) (spiroH₄) and ancillary ligands based on tris(2-pyridylmethyl)amine (tpa) has been synthesized and characterized. The bis(dioxolene) bridging ligand is redox-active and accessible in the (spiro^{cat-cat})⁴⁻, (spiro^{SQ-cat})³⁻, and (spiro^{SQ-SQ})²⁻ forms, (cat = catecholate, SQ = semiquinonate). Variation of the ancillary ligand (Me_ntpa; *n* = 0–3) by successive methylation of the 6-position of the pyridine rings influences the redox state of the complex, governing the distribution of electrons between the cobalt centers and the bridging ligands. Pure samples of salts of the complexes [Co₂(spiro)(tpa)₂]²⁺ (**1**), [Co₂(spiro)(Me₁tpa)₂]²⁺ (**2**), [Co₂(spiro)(Me₂tpa)₂]²⁺ (**3**), [Co₂(spiro)(Me₃tpa)₂]²⁺ (**4**), [Co₂(spiro)(tpa)₂]³⁺ (**5**), and [Co₂(spiro)(tpa)₂]⁴⁺ (**6**) have been isolated, and **1**, **4**, and **6** have been characterized by single crystal X-ray diffraction. Studies in the solid and solution states using multiple techniques reveal temperature invariant redox states for **1**, **2**, and **4–6** and provide clear evidence for four different charge distributions: **1** and **2** are Co^{III}-(spiro^{cat-cat})-Co^{III}, **4** is Co^{II}-(spiro^{SQ-SQ})-Co^{II}, **5** is Co^{III}-(spiro^{SQ-cat})-Co^{III}, and **6** is Co^{III}-(spiro^{SQ-SQ})-Co^{III}. Of the six complexes, only **3** shows evidence of temperature dependence of the charge distribution, displaying a rare thermally induced two-step valence tautomeric transition from the Co^{III}-(spiro^{cat-cat})-Co^{III} form to Co^{II}-(spiro^{SQ-cat})-Co^{III} and then to Co^{II}-(spiro^{SQ-SQ})-Co^{II} in both solid and solution states. This is the first time a two-step valence tautomeric (VT) transition has been observed in solution. Partial photoinduction of the VT transition is also possible in the solid. Magnetic and spectroscopic studies of **5** and **6** reveal that spiroconjugation of the bis(dioxolene) ligand allows electronic interaction across the spiro bridge, suggesting that thermally activated vibronic coupling between the two cobalt-dioxolene moieties plays a key role in the two-step transition evident for **3**.



INTRODUCTION

Molecular species that can be switched between distinguishable electronic states by application of an external stimulus represent an important goal in the miniaturization of materials. The types of molecular systems that can be switched in this manner include spin crossover complexes, heterometallic complexes that show charge-transfer induced spin transitions (CTIST), and valence tautomeric (VT) complexes.^{7,8} Whereas the switching in CTIST species is associated with intramolecular electron transfer between metal centers and the switching in spin crossover complexes is due a spin state transition at a

single metal center, valence tautomerism involves intramolecular electron transfer between a metal and a ligand, often combined with a spin state transition at the metal center. Valence tautomeric transitions have mainly been observed for octahedral cobalt complexes with dioxolene (diox) ligands, for which the electron transfer from a catecholate (cat) ligand to the low spin (LS) cobalt(III) ion triggers a spin transition, yielding a high spin (HS) cobalt(II) ion coordinated to a

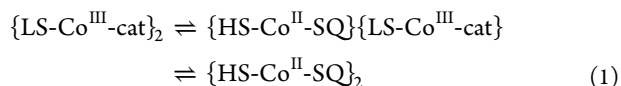
Received: February 27, 2013

Published: May 10, 2013

paramagnetic semiquinonate (SQ) ligand.⁹ These transitions are induced by the application of external stimuli including heat, pressure, magnetic field, or irradiation with visible light or soft X-rays.^{9–12} The thermal induction of the transition is entropically driven, with the large entropy gain arising from the higher density of vibrational states of the HS cobalt(II) complex, due to the longer Co–O/N bond lengths and from the higher spin state degeneracy of this species.

Valence tautomeric transitions are often accompanied by distinct and reversible changes in structural, optical, and magnetic properties, which may afford future applications in molecule-based materials for display devices, high-density data storage, molecular switches or sensors. Of particular interest in this context are bistable materials that display a hysteretic VT transition around room temperature, with a reasonably wide thermal hysteresis loop. Also potentially important for future applications are systems in which a relatively long-lived metastable state can be produced (e.g., photogenerated) at accessible temperatures. For molecular electronics, molecules that can be interconverted between two distinct electronic states hold promise as simple molecular logic gates.¹³ Even more attractive are species that can be interconverted between three distinct electronic states.¹⁴ In particular, interconversion between three different states by two different stimuli (e.g. heat and light) is of interest for more complex logic processes, such as write–lock–read–unlock–erase cycles. In principle, three-state molecular VT systems may be achieved with dinuclear complexes that exhibit distinct VT transitions at each metal center, affording an overall two-step transition. Such systems require that the degree of electronic interaction between the separate VT units is small but nonzero, so that each state can be accessed separately. Analogous two-step spin crossover transitions are well established for dinuclear iron(II) complexes and commonly observed as a plateau in the variable temperature magnetic susceptibility profile.¹⁵ The occurrence of separate LS to HS transitions at each iron(II) center gives rise to the stepwise transition, affording a system that can be accessed in three distinct states (LS–LS, LS–HS, and HS–HS).

A number of dinuclear complexes based on cobalt-dioxolene units have been reported to date, some of which exhibit VT transitions.^{16–19} The only example for which a thermally induced two-step VT transition has been reported is [$\{\text{Co}(3,5\text{-dbdiox})_2\}_2(\text{ppm})$] (ppm = 4,6-di-2'-pyridylpyrimidine), on the basis of variable temperature (88–428 K) near-infrared spectra measured on a thin amorphous film.¹⁸ The two-step transition can be written as

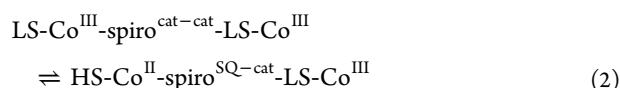


However, this transition is incomplete, with the $\{\text{LS-Co}^{\text{III}}\text{-cat}\}_2$ state not fully realized down to 88 K. Powder and solution samples of this complex were also investigated, and although at least a partial VT transition occurs for all three phases of the complex, the observed behavior is critically dependent on the environment of the cobalt complex. In related systems, the bis(bidentate) tetraoxolene ligand derived from 2,5-dihydroxy-1,4-benzoquinone (d**hbq**) has been used to bridge $\{\text{Co}(\text{tpa})\}$ units (tpa = tris(2-pyridylmethyl)amine) in the dinuclear complex [$\{\text{Co}(\text{tpa})_2(\text{d**hbq**)\}^{3+}$], which exhibits a thermally induced VT transition at one cobalt center, accompanied by wide hysteresis centered at 303 K.^{20,21}

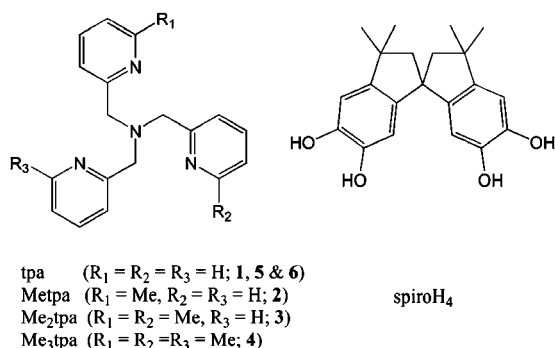
Interestingly the system that exhibits the most definitive two-step VT transition is a mononuclear complex $[\text{Co}(3,5\text{-dbcat})(\text{Me}_2\text{tpa})]^+$ (3,5-d**bc**at = 3,5-di-*tert*-butylcatechol; Me_2tpa = bis(6-methyl-2-pyridylmethyl)(2-pyridylmethyl)amine), with magnetic susceptibility data obtained on a crystalline sample of $[\text{Co}(3,5\text{-dbcat})(\text{Me}_2\text{tpa})](\text{PF}_6)\cdot\text{toluene}$ showing a well-defined plateau and two essentially complete transitions. This behavior is attributed to the presence of two crystallographically independent metal complexes in the sample, which undergo distinct VT transitions at different temperatures, presumably due to different local solvation environments.²² Indeed a considerable body of work has revealed the importance of seemingly secondary structural features, such as intermolecular interactions, counterion, solvation, and ancillary ligand in governing the manifestation of VT transitions.^{21–26}

Of the various ancillary ligands that have been used to generate cobalt-dioxolene complexes that undergo VT transitions, the versatility of tetradentate nitrogen donor ligands derived from tpa has stood out.²⁷ The ready derivatization of tpa allowed Dei and co-workers to elegantly demonstrate the tuning of VT properties in the family of $[\text{Co}(3,5\text{-dbdiox})](\text{Me}_n\text{tpa})^+$ ($n = 0–3$) complexes.²⁸ Sequential addition of methyl groups into the 6-position of the pyridine rings increases the steric hindrance at the cobalt center, thereby modulating its redox properties and controlling the charge distribution across the cobalt-dioxolene unit.²⁷ Magnetic susceptibility measurements in the temperature range 2–320 K indicate a temperature-invariant HS-Co(II)-SQ tautomer for the Me_3tpa complex, while the tpa and Me_2tpa complexes both remain as the LS-Co(III)-cat tautomer throughout this temperature range. In contrast, the Me_2tpa complex showed the onset of a thermally induced VT transition at around 280 K. Photoinduced VT transitions were also evident for the tpa, Me_2tpa , and Me_3tpa complexes. This study has in part prompted the research reported herein, as we were interested in investigating whether we could use similar derivatization of the tpa ligands in dinuclear complexes to achieve a two-step VT transition.

A bis(bidentate) bis(dioxolene) proligand that was immediately appealing for our target two-step VT transition was 3,3,3',3'-tetramethyl-1,1'-spirobis(indane-5,5',6,6'-tetrol) (spiroH₄). Following deprotonation, this ligand is potentially accessible in three redox forms: (spiro^{cat-cat})⁴⁻, (spiro^{SQ-cat})³⁻, and (spiro^{SQ-SQ})²⁻, with the spiroconjugation allowing electronic interaction between the two halves of the ligand.^{29–31} Indeed, a very weak antiferromagnetic interaction between the two semiquinone ($S = 1/2$) units was reported for the dinuclear species $[\text{Co}^{\text{III}}_2(\text{spiro}^{\text{SQ-SQ}})(\text{cth})_2](\text{PF}_6)_4$ (cth = cth = DL-5,7,7,12,14,14-hexamethyl-1,4,8,11-tetraazacyclotetradecane), although the magnitude of the coupling was not provided.⁶ The one electron reduced form of this complex, $[\text{Co}^{\text{III}}_2(\text{spiro}^{\text{SQ-cat}})(\text{cth})_2]^{3+}$, was mentioned in the same report. Several other cobalt complexes of deprotonated spiroH₄ have been reported, although crystals suitable for single crystal X-ray diffraction have proved elusive. These include a mononuclear complex $[\text{Co}^{\text{III}}(\text{spiro}^{\text{SQ-catH}})(\text{cth})]^{2+}$ (with the semiquinonate part of the ligand coordinated to the LS-cobalt(III) center), for which no VT transition was apparent.³² Another compound, believed to be a (spiro^{SQ-cat})³⁻-bridged LS-cobalt(III) 1D polymer, exhibits the beginning of a thermally induced VT transition above 250 K assigned to the following process:³³



Although prior structural data are unavailable for cobalt-spiro complexes, several complexes of $(\text{spiro}^{\text{cat-cat}})^{4-}$ coordinated to other elements have been characterized by single crystal X-ray diffraction, including the discrete molecular species $[\{\text{MoO}_2(\text{spiro})\}_2]^{4-}$, $[\text{B}_4(\text{spiro})_4]^{4-}$, and $[\text{B}_3(\text{spiro})_3]^{3-}$.^{34–36} Herein we report the synthesis and properties in the solid state and in solution of six members of the structural family $[\text{Co}_2(\text{spiro})(\text{Me}_n\text{tpa})_2]^{x+}$: $[\text{Co}_2(\text{spiro})(\text{tpa})_2]^{2+}$ (**1**), $[\text{Co}_2(\text{spiro})(\text{Metpa})_2]^{2+}$ (**2**), $[\text{Co}_2(\text{spiro})(\text{Me}_2\text{tpa})_2]^{2+}$ (**3**), $[\text{Co}_2(\text{spiro})(\text{Me}_3\text{tpa})_2]^{2+}$ (**4**), $[\text{Co}_2(\text{spiro})(\text{tpa})_2]^{3+}$ (**5**), and $[\text{Co}_2(\text{spiro})(\text{tpa})_2]^{4+}$ (**6**). Some aspects of the chemistry of complexes **1**, **3** and **4** in the solid state have been communicated previously.³⁷



RESULTS AND DISCUSSION

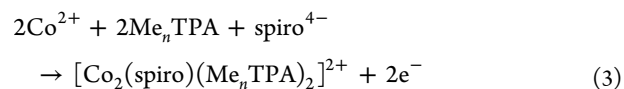
Synthesis. Compounds of four dinuclear cobalt complexes were synthesized with yields higher than 50% by reacting the tetra-deprotonated form of spiroH₄ with 2 equiv of cobalt(II) perchlorate and $(\text{H}_3\text{tpa})(\text{ClO}_4)_3$, $(\text{H}_3\text{Metpa})(\text{ClO}_4)_3$ or Me_ntpa ($n = 2$ or 3).

Following neutralization with triethylamine, a solution of $(\text{H}_3\text{tpa})(\text{ClO}_4)_3$ or $(\text{H}_3\text{Metpa})(\text{ClO}_4)_3$ in warm methanol was combined with a solution of cobalt(II) perchlorate in warm methanol to give a light-brown solution. Addition of tetradeprotonated spiro⁴⁻ caused the solution to turn darker brown, then to green, with the formation of the products as green precipitates. Following recrystallization, the isolated compounds of the complexes $[\text{Co}_2(\text{spiro})(\text{Me}_n\text{tpa})_2]^{2+}$ (**1** and **2** for $n = 0$ and 1 , respectively) were identified as $[\text{Co}_2(\text{spiro})(\text{tpa})_2](\text{ClO}_4)_2 \cdot 6\text{H}_2\text{O}$ (**1a**) and $[\text{Co}_2(\text{spiro})(\text{Metpa})_2](\text{ClO}_4)_2 \cdot 4\text{H}_2\text{O}$ (**2a**). The use of hexafluorophosphate anions afforded a small amount of the compound $[\text{Co}_2(\text{spiro})(\text{tpa})_2](\text{PF}_6)_2 \cdot 4\text{py}$ (**1b**), which was characterized by single crystal X-ray diffraction.

The synthesis of complexes incorporating the Me_ntpa ($n = 2$ and 3) ligands requires the use of anaerobic conditions for the first part of the reaction. Under a nitrogen atmosphere separate methanol solutions of Me_2tpa and cobalt(II) perchlorate were combined. The subsequent addition of spiro⁴⁻ afforded a brown solution. Air was then bubbled into the reaction, turning the solution dark blue, with the precipitation of a blue-green microcrystalline product. Following recrystallization, the isolated compounds of the complexes $[\text{Co}_2(\text{spiro})(\text{Me}_n\text{tpa})_2]^{2+}$ (**3** and **4** for $n = 2$ and 3 , respectively) were identified as $[\text{Co}_2(\text{spiro})(\text{Me}_2\text{tpa})_2](\text{ClO}_4)_2 \cdot 3.5\text{H}_2\text{O}$ (**3a**) and $[\text{Co}_2(\text{spiro})$

$(\text{Me}_3\text{tpa})_2](\text{ClO}_4)_2 \cdot 2\text{H}_2\text{O}$ (**4a**). The use of cobalt(II) chloride in the place of the perchlorate afforded a small amount of the compound $[\text{Co}_2(\text{spiro})(\text{Me}_3\text{tpa})_2][\text{CoCl}_4] \cdot 7\text{MeOH}$ (**4b**), which was characterized by single crystal X-ray diffraction. Despite significant effort, it was not possible to obtain crystals of any salt of complex **3** that diffracted sufficiently well to allow structural determination.

The equation for the reaction that occurs in all four syntheses may be written as



where the oxidizing equivalents are provided by oxygen from air. While complexes **1** and **2** are obtained following reactions performed entirely in air, the synthesis of complexes **3** and **4** requires an anaerobic environment until after both the ancillary Me_ntpa ligands and the redox-active spiro⁴⁻ bridging ligand are combined with the labile cobalt(II) ions. The physical characterization (see later) indicates that while complexes **1** and **2** are in the redox isomeric form $[\text{Co}^{\text{III}}_2(\text{spiro}^{\text{cat-cat}})(\text{Me}_n\text{TPA})_2]^{2+}$, complexes **3** (in solution at least) and **4** display the alternative form $[\text{Co}^{\text{II}}_2(\text{spiro}^{\text{SQ-SQ}})(\text{Me}_n\text{TPA})_2]^{2+}$. Thus the oxygen oxidizes the cobalt centers in the case of complexes **1** and **2** and the bridging spiro ligand in the case of **3** and **4**. The requirement for anaerobic conditions for the formation of **3** and **4** possibly reflects the faster oxidation of the $(\text{spiro}^{\text{cat-cat}})^{4-}$ ligand to $(\text{spiro}^{\text{SQ-SQ}})^{2-}$, versus the slower oxidation of the cobalt(II) centers. Solid samples of compounds **1a–4a** are stable for some weeks when stored in the refrigerator (in the absence of light), although they show signs of turning brown upon lengthy exposure to light, possibly due to photoreduction.

One- and two-electron oxidized derivatives of complex **1**, $[\text{Co}_2(\text{spiro})(\text{tpa})_2]^{3+}$ (**5**) and $[\text{Co}_2(\text{spiro})(\text{tpa})_2]^{4+}$ (**6**) have also been synthesized both chemically and electrochemically, although solid salts were only isolated following chemical oxidation. Cyclic voltammetric studies of **1** (see Electrochemistry section) reveal two accessible oxidation processes associated with sequential oxidation of the bis(dioxolene) ligand from $(\text{spiro}^{\text{cat-cat}})^{4-}$ to $(\text{spiro}^{\text{SQ-cat}})^{3-}$ and then to $(\text{spiro}^{\text{SQ-SQ}})^{2-}$. Oxidation of **1** with just under one equivalent of ferrocenium afforded the brown compound $[\text{Co}_2(\text{spiro})(\text{tpa})_2](\text{PF}_6)_3$ (**5a**). Although it was not possible to obtain crystalline material for X-ray diffraction studies, elemental analysis confirmed the composition and steady-state voltammetry confirmed the redox state. Alternatively, oxidation of **1** with an excess of silver triflate gave the red species $[\text{Co}_2(\text{spiro})(\text{tpa})_2](\text{PF}_6)_4 \cdot 4\text{Me}_2\text{CO}$ (**6b**), which was characterized crystallographically, with the bulk sample analyzing as $[\text{Co}_2(\text{spiro})(\text{tpa})_2](\text{PF}_6)_4 \cdot \text{H}_2\text{O}$ (**6a**). Complex **5** could also be synthesized in much higher yield by a comproportionation reaction between equal amounts of **1** and **6**. Both compounds **5a** and **6a** are also unstable if stored in the light. Bulk samples of compounds **1a–6a** all analyzed satisfactorily for C, H, N, and Cl or P, confirming sample purity and the overall charge of the metal-containing cations.

Structures. As well as unequivocally identifying the molecular structure of the complexes in the solid state, the interatomic distances and angles available from diffraction studies on single crystals are invaluable for the determination of the redox states of the metal centers and ligands in cobalt-dioxolene complexes. The single crystal X-ray diffraction data for compounds **1b**, **4b**, and **6b** are available in Table 1.

Table 1. Crystal Data for Compounds **1b**, **4b**, and **6b**

	1b	4b	6b
empirical formula	C ₇₇ H ₇₆ Co ₂ F ₁₂ N ₁₂ O ₄ P ₂	C ₇₀ H ₉₆ Cl ₄ Co ₃ N ₈ O ₁₁	C ₆₉ H ₈₀ Co ₂ F ₂₄ N ₈ O ₈ P ₄
formula weight/g mol ⁻¹	1641.30	1544.14	1847.15
temperature/K	130(2)	130(2)	130(2)
crystal system	triclinic	monoclinic	orthorhombic
space group	$P\bar{1}$	$P2_1/n$	$Pbca$
crystal size/mm	0.40 × 0.08 × 0.07	0.39 × 0.08 × 0.02	0.27 × 0.21 × 0.02
a/Å	14.400(3)	20.2344(8)	22.8044(9)
b/Å	14.6132(19)	13.0215(5)	41.7897(11)
c/Å	20.424(3)	27.8716(10)	17.9753(9)
α/°	86.927(12)	90	90
β/°	79.811(16)	92.334(3)	90
γ/°	67.788(17)	90	90
V/Å ³	3915.9(12)	7337.6(5)	17130.3(12)
Z	2	4	8
ρ _{calc} /mg m ⁻³	1.392	1.398	1.432
μ/mm ⁻¹	4.451	7.135	4.686
F[000]	1692	3236	7552
θ range/°	3.27–51.47	2.65–51.16	3.30–59.99
reflms measd	13371	26701	36733
unique reflms	8234	7859	12700
data/restraints/parameters	8234/0/827	7859/0/739	12700/2/851
R _{int}	0.0686	0.0575	0.0999
R ₁ [I > 2σ(I)]	0.0887	0.0546	0.1114
wR ₂ (all data)	0.2884	0.1506	0.3312
goodness-of-fit F ²	1.034	1.052	0.986
Δρ _{max,min} /e Å ⁻³	0.769, -0.481	0.420, -0.394	0.816, -0.644

Structural representations of complexes **1** in **1b**, **4** in **4b**, and **6** in **6b** are presented in Figure 1, and selected interatomic distances and angles are provided in Tables 2 and S1, respectively. The formation of single crystals suitable for X-ray diffraction required the use of counteranions other than perchlorate. Single crystal X-ray diffraction analysis at 130 K reveals that complexes **1** in [Co₂(spiro)(tpa)₂](PF₆)₂·4py (**1b**), **4** in [Co₂(spiro)(Me₃tpa)₂][CoCl₄]·7MeOH (**4b**), and **6** in [Co₂(spiro)(tpa)₂](PF₆)₄·4Me₂CO (**6b**) all display similar v-shaped molecular structures with the spiro bridging ligand acting as a hinge between the two halves of the molecule (Figures 1 and S1; Table S1).

A close inspection of the coordination spheres of the cobalt centers for **1** and **6** affords Co–O, Co–N_{amine}, and Co–N_{pyridine} distances in the ranges 1.854(6)–1.911(5), 1.921(7)–1.972(7), and 1.868(10)–1.940(8) Å, respectively (Table 2). These distances are consistent with two LS-cobalt(III) centers in these two complexes. In contrast, the Co–O/N distances observed for **4** are longer, with Co–O, Co–N_{amine}, and Co–N_{pyridine} distances of 1.994(4)–2.104(4), 2.105(4), and 2.140(5)–2.252(5) Å, respectively, consistent with two HS-cobalt(II) centers. The redox state of dioxolene ligands can often be determined from a consideration of the C–O and (O)C–C(O) bond distances.³⁸ For **1** the C–O distances are 1.353(11)–1.374(11) Å and the (O)C–C(O) distances are 1.414(13)–1.415(14) Å, suggesting that both dioxolene moieties are in the catecholate state. For complexes **4** and **6** the C–O distances are in the range 1.278(9)–1.337(11) Å and the (O)C–C(O) distances are 1.465(12)–1.474(8) Å, consistent with both dioxolene moieties are in the semiquinonate state (Figure S1). These bond lengths were further parameterized by calculation of Carugo's parameter Δ, which takes values of –1 and –2 for pure semiquinonate and

catecholate ligands, respectively.^{38a} The Δ parameters were calculated to be –2.1 and –1.9 for **1**, –1.2 and –0.97 for **4**, and –1.1 and –1.2 for **6**, consistent with the assignments of the redox states of the ligands made by bond length inspection. Thus the key bond lengths derived from X-ray crystallography data at 130 K indicate three different electronic distributions for the three complexes: LS-Co^{III}-(spiro^{cat-cat})-LS-Co^{III} for complex **1** in compound **1b**, HS-Co^{II}-(spiro^{SQ-SQ})-HS-Co^{II} for complex **4** in compound **4b**, and LS-Co^{III}-(spiro^{SQ-SQ})-LS-Co^{III} for complex **6** in compound **6b**.

While the dinuclear complexes **4** in **4b** and **6** in **6a** both display pseudo two-fold symmetry, complex **1** in **1b** is asymmetric, with two chemically distinct cobalt centers. This is readily apparent from a consideration of the bond *trans* to the amine nitrogen of the tpa ligands, which for one, the cobalt center is occupied by the dioxolene oxygen atom proximal to the spirocyclic carbon and for the other, it is occupied by the distal oxygen atom. In contrast, for **4** and **6** the bond *trans* to the amine nitrogen of the tpa ligands is occupied by the oxygen atom proximal to the spirocyclic carbon. As **6** is synthesized by oxidation of **1** and both complexes contain substitutionally inert LS-Co(III) centers, the bulk sample of both complexes probably contains both symmetric and asymmetric isomers.

The considerable flexibility of the spiro ligand as a hinge is apparent from its position at the vertices of both square- and triangular-shaped complexes in [MoO₂(spiro)]₂⁴⁺, [B₄(spiro)₄]⁴⁺, and [B₃(spiro)₃]^{3–34–36}. Flexibility is also evident in the structures of **1**, **4**, and **6**, with the geometry at the spirocyclic carbon playing a key role in determining the relative orientation of the two halves of the molecule with respect to each other and therefore the electronic communication between them. Comparison of the important angles relating the two halves of the complexes through spirocyclic

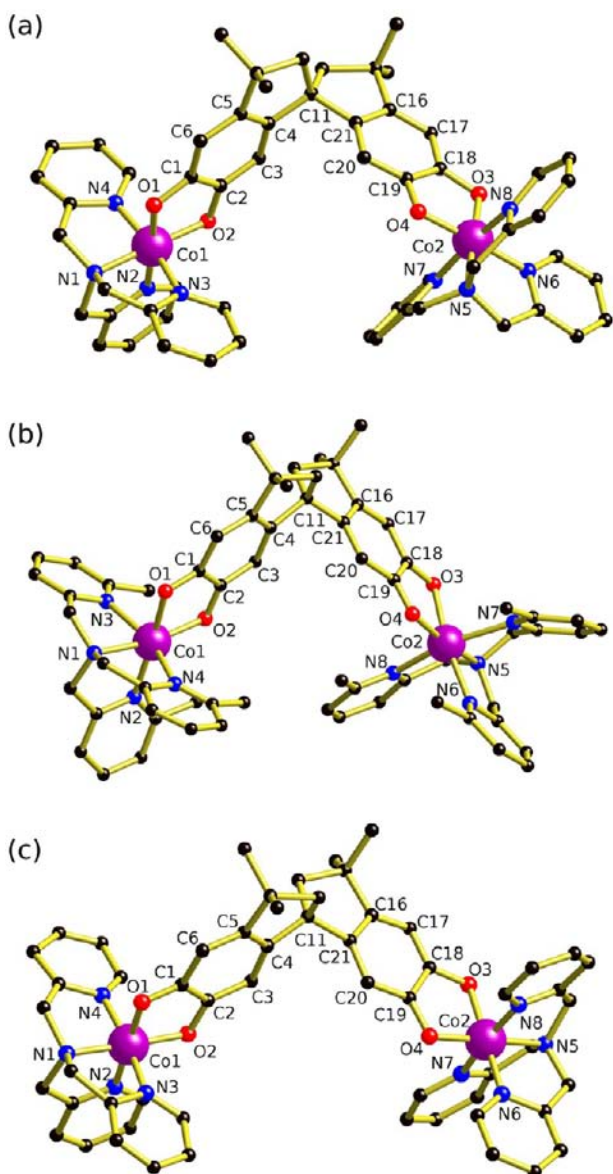


Figure 1. Structural representations of complexes (a) **1** in **1b**, (b) **4** in **4b**, and (c) **6** in **6b**.

carbon atom is provided in Table 2. For a strictly sp^3 carbon the $C4-C_{\text{spiro}}-C21$ and dihedral angles should be 109.5° and 90° , respectively. Deviations from these values are apparent in all three complexes, and most pronounced for complex **6**. The further away from the spirocyclic carbon, the more pronounced is the effect of the deviation, for instance by consideration of the 1 \AA longer intermetallic separation for **6** versus **1** and **4**. This increase for **6** is likely due to the presence of a hexafluorophosphate counteranion in the middle of the “v”, which displays multiple intermolecular $F \cdots H-C$ hydrogen bonds to the tpa ligands from the two halves of the complex (Figure S2).

Infrared Spectroscopy. Infrared spectroscopy can be helpful for distinguishing catechol and semiquinone moieties, particularly upon consideration of the relatively intense absorptions between 1250 and 1650 cm^{-1} associated with $C-O$ stretching modes. A detailed experimental and theoretical study of the solution infrared spectra of $[\text{Co}^{\text{III}}(3,5\text{-dbcat})(\text{tpa})]\text{PF}_6$ and $[\text{Co}^{\text{II}}(3,5\text{-dbSQ})(\text{Me}_3\text{tpa})]\text{PF}_6$ provides

Table 2. Selected Interatomic Distances and Angles for Complexes **1** in **1b**, **4** in **4b**, and **6** in **6b**

	1	4	6
Distances / \AA			
Co1...Co2 ^a	9.565(2)	9.497(1)	10.465(4)
Co1–O1	1.869(6)	2.101(4)	1.911(5)
Co1–O2	1.868(6)	1.994(4)	1.854(6)
Co1–N1 ^b	1.933(8)	2.105(5)	1.921(7)
Co1–N2	1.940(8)	2.149(5)	1.910(7)
Co1–N3	1.939(8)	2.243(5)	1.905(8)
Co1–N4	1.907(8)	2.210(5)	1.893(6)
Co2–O3	1.868(7)	2.104(4)	1.894(8)
Co2–O4	1.883(7)	2.008(4)	1.875(5)
Co2–N5 ^b	1.944(9)	2.105(4)	1.972(7)
Co2–N6	1.926(9)	2.140(5)	1.868(10)
Co2–N7	1.926(8)	2.252(5)	1.908(6)
Co2–N8	1.936(8)	2.210(5)	1.890(6)
O1–C1	1.356(11)	1.288(6)	1.278(9)
O2–C2	1.353(10)	1.287(6)	1.302(8)
O3–C18	1.353(11)	1.280(6)	1.337(11)
O4–C19	1.374(11)	1.284(6)	1.293(10)
C1–C2	1.414(13)	1.468(8)	1.465(10)
C1–C6	1.394(13)	1.423(8)	1.458(10)
C2–C3	1.387(13)	1.410(8)	1.411(10)
C3–C4	1.385(13)	1.382(7)	1.383(11)
C4–C5	1.367(14)	1.409(7)	1.416(11)
C5–C6	1.420(14)	1.365(7)	1.364(11)
C16–C17	1.382(13)	1.358(7)	1.341(13)
C16–C21	1.393(14)	1.427(8)	1.414(12)
C17–C18	1.392(13)	1.429(8)	1.340(13)
C18–C19	1.415(14)	1.474(8)	1.465(12)
C19–C20	1.371(13)	1.422(7)	1.427(10)
C20–C21	1.392(13)	1.377(7)	1.366(12)
Angles / $^\circ$			
$C4-C_{\text{spiro}}-C21$	112.8(8)	112.2(4)	115.7(8)
Co1– C_{spiro} –Co2	95.5	92.0	108.5
dihedral angle ^c	90.7	90.3	92.9

^aIntramolecular distance between the cobalt centers. ^bN1 and N5 correspond to the aliphatic tertiary amine N atom of the Me_nTPA terminal ligand ($n = 0$ and 3). ^cAngle between the two planes is defined as carbon atoms ($C4$, $C10$, and $C11$ (spirocyclic)) and ($C11$ (spirocyclic), $C12$, $C21$).

invaluable insights into the present study.³⁹ Infrared spectra of pressed KBr disks of compounds **1a–6a** are available in Figures 2 and S3. The spectra measured for the unoxidized compounds **1a–4a** show a clear decrease in intensity of spectral characteristics associated with catechol and a concomitant increase in intensity of bands associated with semiquinone, with increasing methylation of the tpa ancillary ligand. In fact, while the spectra of **1a** and **2a** are characteristic of catechol complexes and the spectrum of **4a** suggests semiquinone characteristics, the spectrum of **3a** shows bands attributable to both catechol and semiquinone units. For example, a strong band assigned to the catechol skeletal dioxolene evident at 1280 cm^{-1} for **1a** and **2a** has a decreased intensity for **3a** and is absent for **4a**. Similarly, while the spectra for compounds **1a** and **2a** exhibit a band at around 1444 cm^{-1} , attributed predominantly to a $C=O$ stretch, and a band at 1454 cm^{-1} mainly due to a $C=O$ stretch is evident for **4a**, compound **3a** exhibits both bands. Finally two bands in the range $1570\text{--}1615 \text{ cm}^{-1}$ assigned as due to $C=C$ stretches increase significantly in

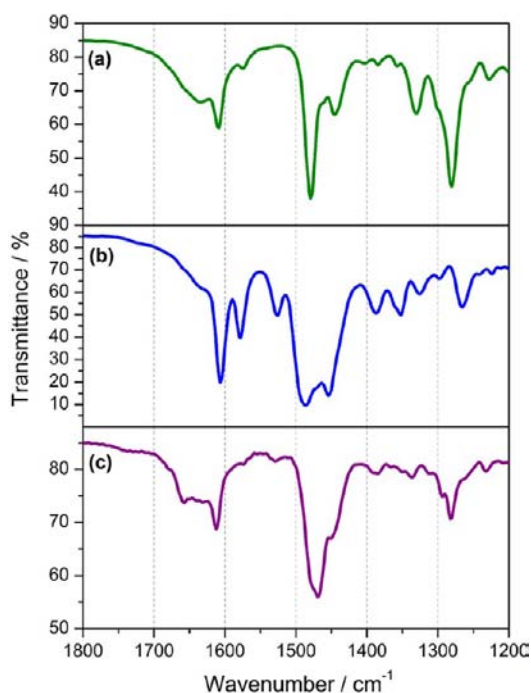


Figure 2. Infrared spectra of pressed KBr disks of compounds (a) **1a**, (b) **4a**, and (c) **6a**.

intensity (and also decrease in separation) of the order **1a** < **2a** < **3a** < **4a**. The infrared spectra of compounds **5a** and **6a** are also broadly consistent with the presence of semiquinone ligands in **6a** and both catechol and semiquinone ligands in **5a**, although there are additional spectral changes of uncertain origin.

Electronic Absorption Spectroscopy. Electronic absorption spectra in the UV–vis range for acetonitrile solutions of compounds **1a**–**6a** are presented in Figure 3. All spectra remained unchanged over a period of several hours, indicating the solution stability of the complexes over this time scale at room temperature. Examination of the spectral features provides insights into the electronic state of the cobalt-dioxolene complexes in solution. Spectral similarities are observed for the pairs of complexes **1** and **2**, **3** and **4**, and **5** and **6**. The solutions of complexes **1** and **2** are green and show electronic transitions consistent with the LS-Co(III)-cat chromophores evident in the solid state.⁴⁰ Broad absorption bands centered on 717 (molar extinction coefficient, $\epsilon = 437 \text{ M}^{-1} \text{ cm}^{-1}$) and 768 nm ($\epsilon = 505 \text{ M}^{-1} \text{ cm}^{-1}$) for **1** and **2**, respectively, are consistent with symmetry-forbidden ligand to metal charge transfer (LMCT) transitions. The very broad shoulders between 430 and 500 nm can be attributed to the d–d transitions ($^1A_{1g} \rightarrow ^1T_{1g}$ of O_h), which are often seen for six coordinate cobalt(III) complexes. A very broad shoulder around 350 and 430 nm has been assigned to LMCT from the catechol π^* orbital. The spectra for blue-green solutions of complexes **3** and **4** are very similar to each other and consistent with the HS-Co(II)-SQ form.⁴¹ A broad shoulder centered on 780 nm has been assigned to internal ligand transitions within the spiro ligand, while sharp bands at around 400 nm have been assigned as an internal $\pi \rightarrow \pi^*$ transition occurring in the semiquinone moiety. The peak pattern observed between 500 and 750 nm has been assigned as metal to ligand charge transfer (MLCT) bands from cobalt(II) to the singly occupied π^* orbital of the semiquinone form of

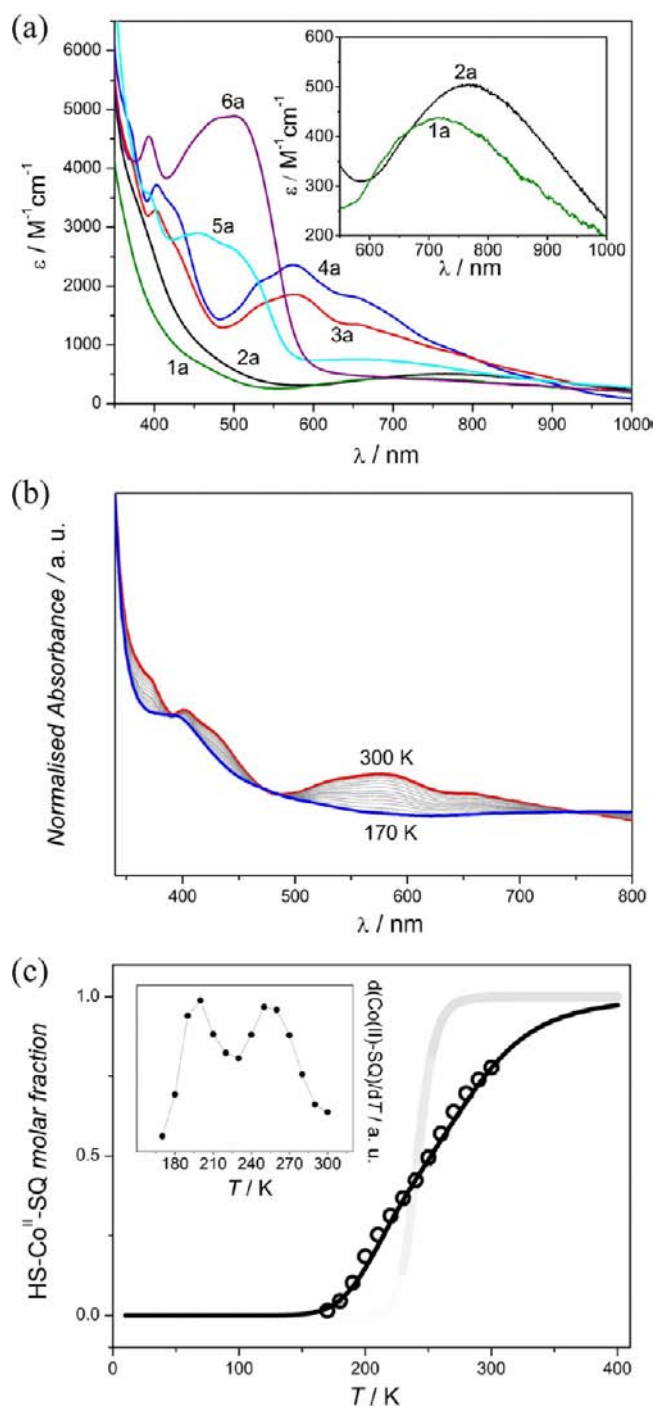


Figure 3. (a) Electronic absorption spectra of solutions of compounds **1a**–**6a** in acetonitrile. (b) Variable temperature (170–300 K) normalized electronic spectra for a solution of compound **3a** in butyronitrile. (c) Temperature dependence of the molar fraction of Co(II)-SQ (%) along with line of best fit (black line), calculated as described in the text; the fading gray band presents the thermal evolution of the EPR spectra of **5a** in acetonitrile/dichloromethane solution, as described in the text. Inset: first derivative plot $d(\text{Co(II)-SQ})/dT$, highlighting the different transition temperatures of the two cobalt-dioxolene moieties connected through the spiro bridge.

the spiro ligand. The spectra for complexes **1**–**4** are very similar to those reported for the mononuclear analogues $[\text{Co}(3,5\text{-dbdiox})(\text{Me}_n\text{tpa})](\text{PF}_6)$,²⁸ with the spectra measured for **1a** and **2a** similar to those of $[\text{Co}^{\text{III}}(3,5\text{-dbcat})(\text{Me}_n\text{tpa})]^+$ ($n = 0$ and

1), while the spectra of **3a** and **4a** resemble those reported for $[\text{Co}^{\text{II}}(3,5\text{-dbSQ})(\text{Me}_n\text{tpa})]^+$ ($n = 2$ and 3).

The spectra obtained for the red-brown one- and two-electron oxidized complexes **5** and **6** differ significantly from that of the parent complex **1**. The broad band relating to the symmetry-forbidden LMCT seen at 717 nm for **1** shifts to higher energy (665 nm) for **5** and disappears altogether for **6**, consistent with the absence of the LS-Co(III)-cat chromophore. The internal $\pi \rightarrow \pi^*$ semiquinonate transitions evident for **3** and **4** are also present for **5** and **6** at 392 ($\epsilon = 3579 \text{ M}^{-1} \text{ cm}^{-1}$) and 393 nm ($\epsilon = 4543 \text{ M}^{-1} \text{ cm}^{-1}$). More notable is the intense new broad band centered around 481 ($\epsilon = 2737 \text{ M}^{-1} \text{ cm}^{-1}$) and 492 nm ($\epsilon = 4873 \text{ M}^{-1} \text{ cm}^{-1}$) for **5** and **6**, respectively. Comparison with previously reported cobalt(III)- and chromium(III)-semiquinonate complexes allows assignment of this band to MLCT between trivalent metal centers and semiquinone moieties.^{19,40,42} The changes in the spectra that occur as **1** is oxidized to **5** and then to **6** reflect the sequential replacement of both LS-Co(III)-cat chromophores with cobalt(III)-semiquinonate moieties, consistent with oxidation of the bridging ligand from (spiro^{cat-cat})⁴⁻ to (spiro^{SQ-SQ})²⁻ in **6**.

In order to gain insights into the entropy driven VT transition of **3a** in solution, variable temperature spectra (Figure 3b) have been collected in the temperature range 170–300 K. To do this, a butyronitrile (freezing point, 161 K) solution was prepared, showing a room temperature electronic spectrum superimposable with the one obtained from an acetonitrile solution (Figure S4a). This suggests that the VT equilibrium is not affected by changing between these two solvents. Comparison of the molar extinction coefficient of **3a** at 574 nm with the ones found for **1a** and **4a** systems (Figure 3a), bearing temperature-independent LS-Co^{III}-Cat and HS-Co^{II}-SQ charge distributions, respectively, reveals the presence of a molar fraction of HS-Co^{II}-SQ, $x_{\text{HS-Co(II)-SQ}} = 0.78$ in solution at room temperature. Upon cooling, the broad MLCT bands between 500 and 750 nm gradually decrease in intensity, while close inspection of the broad band centered around 770 nm shows a small increase, suggesting the onset of the symmetry-forbidden LMCT peculiar to the cobalt(III)-catecholate chromophore. The broad shoulder and peak between 350 and 500 nm, present at 300 K, also decrease in intensity upon cooling, and at 170 K the solution spectrum of **3a** resembles the room temperature spectra measured for the LS-Co(III)-cat complexes **1** and **2**. Visual inspection of the chilled sample suggested that there was no significant precipitation induced by cooling. The absorption spectra obtained upon heating the solution back to 300 K match the ones measured upon cooling, indicating that the observed transition is reversible. After spectral normalization to remove scattering effects due to partial aggregation at low temperatures, isosbestic points are found at 390, 471, 486, 750, and 832 nm, indicating that the transition in the range 170–300 K involves only two different chromophores. Interestingly, the thermal variation of the fraction of HS-Co(II)-SQ determined by spectral deconvolution (using the 170 and 300 K ones as limiting compositional references for the LS-Co(III)-cat and HS-Co(II)-SQ, respectively) appears to follow a double sigmoidal profile. Its derivative plot confirms this (Figure 3c inset), revealing two maxima centered around 200 and 250 K, implying a gradual two-step transition in solution. A similar result was obtained through the comparison of the extinction coefficients at 574 nm (Figure 3c); however, the transition

profile in solution has been extrapolated by the deconvolution procedure, since this relies on the whole investigated spectral range rather than on a single point measurement.

The thermodynamic parameters governing the two distinct transitions of **3a** have been obtained with a least-squares fit of the thermal distribution curve of the HS-Co^{II}-SQ molar fraction, using a model featuring two noninteracting Boltzmann distributions of HA-Co(II)-SQ:^{17,43}

$$x_{\text{HS-Co}^{\text{II}}\text{-SQ}} = \frac{1}{2} \left[\frac{1}{(e^{\Delta H_1/RT} \cdot e^{-\Delta S_1/R} + 1)} + \frac{1}{(e^{\Delta H_2/RT} \cdot e^{-\Delta S_2/R} + 1)} \right] \quad (4)$$

where ΔH_1 , ΔH_2 , ΔS_1 , and ΔS_2 are the enthalpic and entropic variations of the two cobalt-dioxolene moieties involved in the VT process. This approach provides a good fit of the experimental data ($R^2 = 0.998$), reported in Figure 3c as a black line, using the parameters $\Delta H_1 = 17(1) \text{ kJ mol}^{-1}$, $\Delta S_1 = 84(7) \text{ J K}^{-1} \text{ mol}^{-1}$ for the first interconverting cobalt center and $\Delta H_2 = 25(2) \text{ kJ mol}^{-1}$ and $\Delta S_2 = 89(9) \text{ J K}^{-1} \text{ mol}^{-1}$ for the other one. These values are in line with previously investigated VT interconversions in solution,^{44–48} and reveal a difference in enthalpy to be the origin of the two-step thermal behavior of **3a**. Attempts to fit the thermal distribution curve with a single VT transition (Figure S4b) give a poorer fit ($R^2 = 0.994$) and thermodynamic parameters outside the expected range for cobalt-dioxolene complexes ($\Delta H = 13.7(4) \text{ kJ mol}^{-1}$ and $\Delta S = 57(2) \text{ J K}^{-1} \text{ mol}^{-1}$) and were thus discarded.

To the best of our knowledge, this is the first experimental evidence for a two-step VT transition in solution. Previously reported two-step VT transitions have been observed in the solid state, with the steps arising from solid-state effects, such as inequivalence of Co-dioxolene sites in the crystal lattice or changes in packing when moving from powder to the film phase.^{17,22} In dinuclear spin crossover systems, two-step transitions are usually considered to arise from intramolecular (magnetic exchange) and/or intermolecular (different coordination environment of the interconverting ions, elastic interactions in the crystal lattice) interactions.⁴³ For **3a** in solution, precipitation upon cooling can be discarded as the origin of the two-step transition, as no significant precipitation or sudden decrease in the measured absorbance was observed, and the signal-to-noise ratio was essentially constant throughout the measured temperature range. Crystal packing effects are not relevant in solution, and thus the 8 kJ mol⁻¹ difference in the enthalpic contributions of the two distinct cobalt-dioxolene centers must be due to intramolecular properties. We can safely discard magnetic exchange energy as the main origin of this difference, since the spiro bridge is found to transmit a coupling interaction of 8 cm⁻¹ (which only corresponds to a 46 J mol⁻¹ energy difference between the differently coupled states of two $S = 1/2$ centers) in the Co^{III}-(spiro^{SQ-SQ})-Co^{III} compound **6a** (see Magnetochemistry section). As described in more detail later, the temperature dependence of the EPR spectra of Co^{III}-(spiro^{SQ-cat})-Co^{III} compound **5a** suggests a thermally induced increase of the vibronic coupling of the two Co-dioxolene moieties linked through the spiro bridge (see EPR Spectroscopy section). This phenomenon takes place in the narrow temperature range of 220–260 K (EPR thermal profile of **5a** depicted in Figure 3c as a gray fading band), which falls in the middle of the VT conversion evident for **3a**. The coincidence of

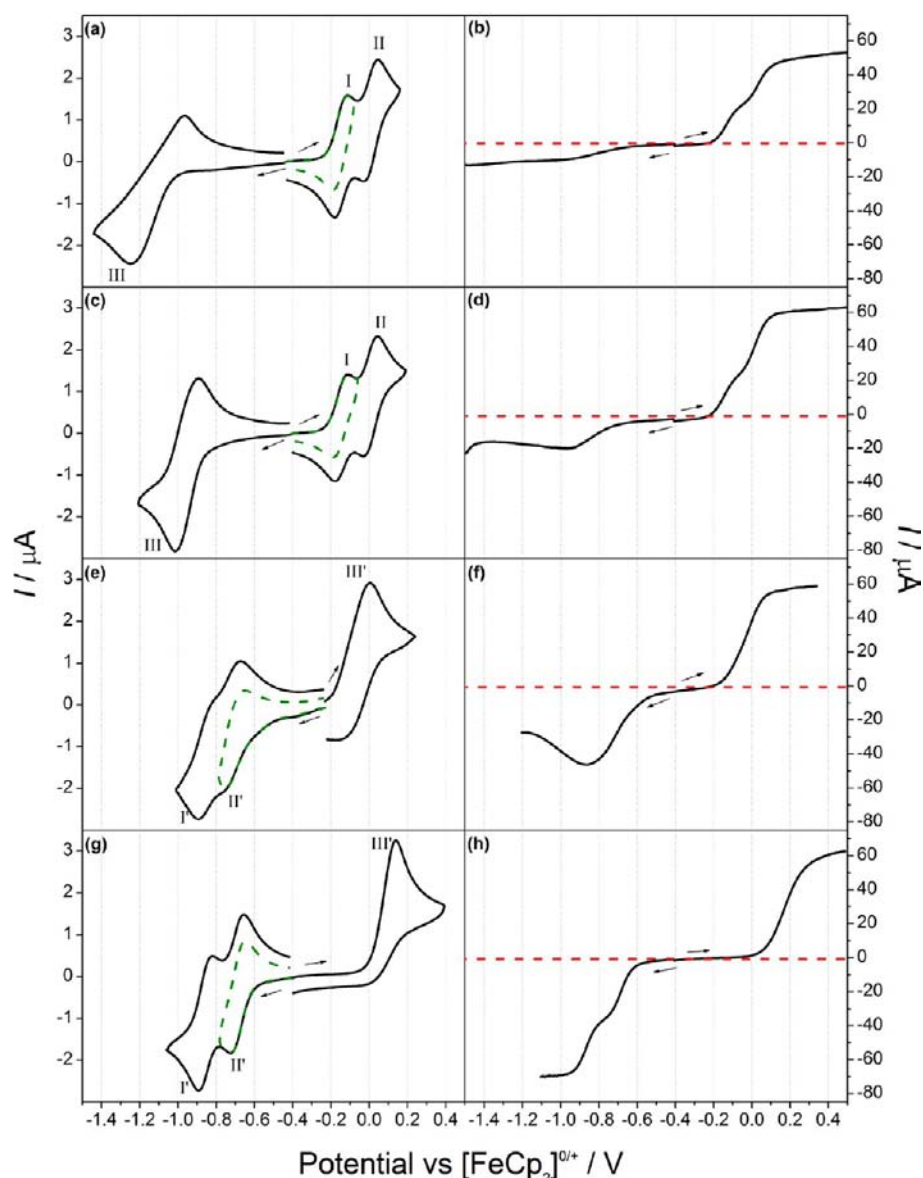


Figure 4. Voltammograms of acetonitrile solutions (1.0 mM with 0.1 M Bu_4NPF_6) of compounds (a and b) **1a**, (c and d) **2a**, (e and f) **3a** and (g and h) **4a** (1.0 mM with 0.1 M Bu_4NPF_6): (left) cyclic voltammograms at a scan rate of 100 mV s^{-1} ; (right) RDE voltammograms at a scan rate of 20 mV s^{-1} and rotation speed of 1000 rpm .

Table 3. Electrochemical Data for Acetonitrile (0.1 M Bu_4NPF_6) Solutions of Compounds 1a–4a^a

redox process	cyclic voltammetry data				RDE voltammetry data			
	E_m or E_p/V , ($\Delta E_p/mV$)				$E_{1/2}/V$, ($i_c/\mu A$)			
	1a	2a	3a	4a	1a	2a	3a	4a
I (I')	−0.153 (75)	−0.150 (80)	−0.711 (80)	−0.685 (75)	−0.135 (28.0)	−0.146 (27.4)	–	−0.868 (32.9)
II (II')	0.008 (75)	0.008 (75)	−0.854 (85)	−0.858 (80)	0.0330 (26.4)	0.0160 (31.6)	–	−0.684 (33.3)
III (III')	−1.11 (285)	−0.953 (125)	0.004 ^b	0.138 ^b	–	–	−0.021 (56.6)	0.168 (62.6)
IV	−2.46 ^b	−2.48 ^b	−2.48 ^b	−2.50 ^b	–	–	–	–
V	0.863 (215)	0.873 (215)	0.984 ^b	–	–	–	–	–

^aAll potentials are referenced versus the ferrocene/ferrocenium couple. ^b E_p rather than E_m .

the temperature ranges over which the two features occur suggests the thermally induced increase of the vibronic coupling between the two interconverting centers to be the origin of the 8 kJ mol^{-1} enthalpic difference in **3a**. A similar ligand-driven regulation of the thermodynamics of interconverting centers

has been previously reported for a dinuclear iron(II) spin crossover system, where ligand rearrangement following the switch of the first iron(II) center led to a $18(11) \text{ kJ mol}^{-1}$ increase of the enthalpy of conversion of the second iron center.⁴⁹

Electrochemistry. Following the confirmation of solution stability by electronic absorption spectroscopy, cyclic voltammograms were measured using a glassy carbon electrode for solutions of compounds **1a–4a** in acetonitrile to probe the redox properties of the cobalt-dioxolene complexes (Figures 4 and S5; Table 3). As per the electronic spectra, compounds **1** and **2** displayed closely related results that differ to those displayed by **3** and **4**, which were again similar to each other. Steady-state voltammograms were obtained for the four compounds using a glassy carbon rotating disk electrode (RDE) (Figure 4), and controlled potential electrolysis experiments were performed on solutions of compounds **1a** and **4a** and monitored by near steady-state voltammetry using a platinum disk microelectrode.

Cyclic voltammetry for **1a** and **2a** revealed over narrow (Figure 4) and wide potential ranges (Figure S5) a total of three resolved oxidation processes (labeled I, II and V) and two reduction processes (labeled III and IV). The midpoint potentials (E_m) tabulated in Table 3 were calculated by taking the average of the oxidation and reduction peak potentials (E_p) from the cyclic voltammograms. Where possible, the peak-to-peak separations (ΔE_p) are also tabulated. The position of zero current in the RDE voltammograms for **1a** and **2a** (Figure 4, right) confirms that processes I, II, and V (not shown) are oxidations, while III and IV (not shown) are reductions. Where possible, the half-wave potentials ($E_{1/2}$) and limiting current values (i_L) from RDE voltammetry are also presented in Table 3. The first two oxidations (I and II) are chemically reversible and diffusion controlled one-electron processes. In the cyclic voltammograms the ratio of oxidative and reductive currents for these processes is close to unity, and the ΔE_p values at a scan rate of 100 mVs^{-1} are less than 85 mV , while the RDE voltammograms display limiting currents (i_L) in the range $26\text{--}32 \text{ mA}$. Coulometry during controlled potential electrolysis for **1a** (see Spectroelectrochemistry and Bulk Electrolysis section) confirms that I and II are both one-electron processes, with the electronic absorption spectroscopy indicating they are ligand based. Thus processes I and II are assigned to the reversible stepwise one-electron oxidation of each half of the spiro ligand from $(\text{spiro}^{\text{cat-cat}})^{4-}$ to $(\text{spiro}^{\text{SQ-SQ}})^{2-}$ (Scheme 1). This assignment of these processes as ligand-based is confirmed by

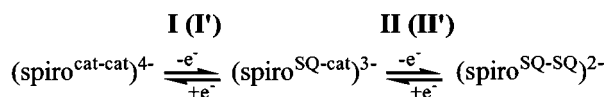
the single-crystal X-ray diffraction structure obtained for the two-electron oxidized form (see Structure section). The third oxidation process V (Figure S5) shows some degree of chemical reversibility and is likely due to further oxidation of the ligand. The cyclic voltammograms suggest the first reduction process III is chemically reversible, with the large ΔE_p and current magnitude relative to processes I and II, suggesting the overall transfer of more than one electron in unresolved steps. The peak shape of the RDE voltammograms indicates precipitation or adsorption associated with process III (to a greater extent for **1a** than **2a**). Thus process III is assigned to two closely spaced one-electron reductions of both cobalt(III) centers to cobalt(II), indicated as processes IIIa and IIIb in Scheme 1. Reductive controlled potential electrolysis (see Spectroelectrochemistry and Bulk Electrolysis section) confirms that process III involves the transfer of two electrons. The second reduction process IV (Figure S5) is essentially irreversible and is likely due to the further reduction of the cobalt centers.

The cyclic voltammograms for **3a** and **4a** (Figures 4 and S5) show a reverse in the relative potentials of processes I–III, now labeled I'–III' for clarity, consistent with the different redox states of complexes **3** and **4** versus **1** and **2**, with the position of zero current in the RDE voltammograms confirming I' and II' as reductions and III' as an oxidation. For **4a**, cyclic voltammetry indicates that processes I' and II' are chemically reversible and diffusion controlled one-electron processes. The i_L values of approximately 33 mA for RDE voltammograms of I and II, respectively, are close to the values obtained for the equivalent processes in **1a** and **2a** as required for the transfer of one-electron per process. For **3a**, the peak shape evident in RDE voltammograms of processes I' and II' suggests associated precipitation or adsorption is coupled to electron transfer. Coulometric analysis of the reductive electrolysis of **4a** (see Spectroelectrochemistry and Bulk Electrolysis section) confirms processes I' and II' involve one-electron charge-transfer steps. Thus, processes II' and I' can be assigned to two sequential, chemically reversible, one-electron reductions, assigned as stepwise reductions of the spiro ligand from $(\text{spiro}^{\text{SQ-SQ}})^{2-}$ to $(\text{spiro}^{\text{cat-cat}})^{4-}$ (Scheme 1). Cyclic voltammograms of process III' for **3a** and **4a** show a loss of chemical reversibility, with this process being completely irreversible for **4a**. Nevertheless the i_L values of 56.6 and 62.6 mA from the RDE voltammograms for **3a** and **4a**, respectively, indicate that process III' involves the transfer of two electrons for **3** and **4**, as for **1** and **2**. Coulometry during oxidative electrolysis (see Spectroelectrochemistry and Bulk Electrolysis section) also indicates that process III' involves the transfer of two electrons. Thus process III' is assigned as the irreversible two-electron oxidation of both cobalt(II) centers to cobalt(III) (Scheme 1). In addition, process IV remains in the same position for the four compounds, consistent with its assignment as due to further reduction of the cobalt centers from cobalt(II), probably to cobalt(I). Finally, process V is evident in the cyclic voltammogram of **3a** at the same potential as for **1a** and **2a**, although the current magnitude is less and a greater level of irreversibility is present, while this process is absent for **4a** up to the solvent limit. These observations are consistent with the increasing irreversibility of process III' for **3a** and **4a**.

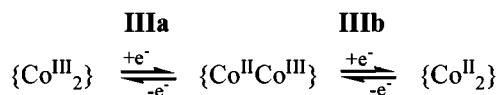
The redox potentials for the ligand-based processes I (I') and II (II') vary little for the pairs of compounds **1a** and **2a** (oxidations) and **3a** and **4a** (reductions). However, the redox potential of the overall two-electron metal based-process III

Scheme 1. Electrochemical Processes I–III (I'–III') for Compounds 1a–4a

ligand-based processes for **1a**, **2a**, **3a** and **4a**:



metal-based processes for **1a** and **2a**:



metal-based processes for **3a** and **4a**:



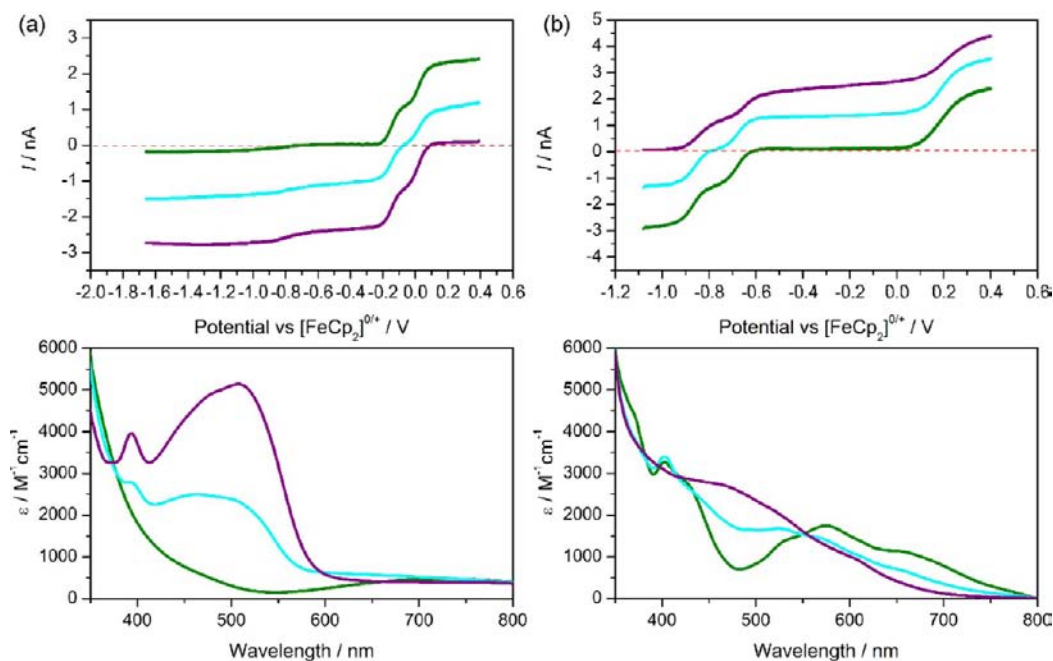


Figure 5. (top) Near steady-state microelectrode linear sweep voltammograms of acetonitrile solutions of (a) **1a** and (b) **4a** (1 mM with 0.1 M Bu₄NPF₆) before electrolysis (green) and after one- (blue) and two-electron (purple) controlled potential electrolyses via processes I (I') and II (II') (oxidation for **1** and reduction for **4**). (bottom) Corresponding electronic absorption spectra.

(III') shifts monotonically to more positive values in the order **1a** < **2a** < **3a** < **4a**. This shift is similar to those observed for the families of copper complexes [Cu(H₂O)(Me_ntpa)]^{2+/+} and [CuCl(Me_ntpa)]⁺⁰ ($n = 0-3$), where the reversible potential of the copper(II)/copper(I) couple shifts in a similar manner.⁵⁰ This shift directly reflects the steric impact of the methyl substituents on the tpa ligands on the size, and therefore oxidation state, of the metal centers. A similar shift can be deduced from the data reported for the [Co(3,5-dbdiox)-(Me_ntpa)]⁺ family of complexes. In addition, the degree of chemical reversibility of process III (III') varies across the four complexes, although the origin of this is not known.

Spectroelectrochemistry and Bulk Electrolysis. Spectroelectrochemical studies were performed on the Co^{III}-(spiro^{cat-cat})-Co^{III} compound **1a** (Figure 5a) in acetonitrile using a platinum-gauze working electrode in an inert atmosphere glovebox. The progress of the electrolyses was monitored coulometrically and with near steady-state microelectrode voltammetry, and the electronic absorption spectra in the UV-vis range were measured *ex situ*. The spectra obtained following one- and two-electron oxidation of **1a** through ligand-based processes I and II (Figure 5a) are essentially identical to the spectra obtained for the chemically oxidized and isolated species **5a** and **6a** (Figure 3a) and consistent with the proposed redox states of Co^{III}-(spiro^{SQ-cat})-Co^{III} and Co^{III}-(spiro^{SQ-SQ})-Co^{III}, following respective one- and two-electron oxidation. Coulometry indicates that electrochemical reduction through metal-based process III involves the transfer of two-electrons to generate a brown Co^{II}-(spiro^{cat-cat})-Co^{II} species (Figure S6). With little literature precedent of cobalt(II)-catecholate species, a definitive assignment of the relatively featureless electronic absorption spectrum is difficult, although the absorption bands attributed to semiquinone-based transitions evident in the spectra of the other semiquinone-containing species are absent in this spectrum. During the course of the reduction, a brown precipitate began to appear, which is possibly the neutral

complex [Co₂(spiro)(tpa)₂], and precipitation continued after the electrolysis was finished. Interestingly it was possible to fully reoxidize this mixture and obtain the original complex **1**, with the precipitated reduced compound redissolving upon the application of an oxidative potential. This implies that the dinuclear complex remains essentially intact throughout.

The proximity of the ligand-based oxidation processes I and II, and the ability to isolate one-electron oxidized complex **5** from a comproportionation reaction between unoxidized **1** and two-electron oxidized **6**, prompted determination of the relevant comproportionation constant.⁵¹ The difference in $E_{1/2}$ values ($\Delta E_{1/2}$) between these processes is 168 mV which indicates a comproportionation constant (K_{comp}) value of 775 (since $\log(K_{\text{comp}}) = 17.2 \times \Delta E_{1/2}$).

In analogous spectroelectrochemical studies on the Co^{II}-(spiro^{SQ-SQ})-Co^{II} compound **4a** (Figure 5b), one- and two-electron reduction through ligand-based processes I' and II' afforded air-sensitive brown Co^{II}-(spiro^{SQ-cat})-Co^{II} and red-brown Co^{II}-(spiro^{cat-cat})-Co^{II} species, respectively. The electronic absorption spectra of two-electron reduced **4** and two-electron reduced **1** are similar (Figures 5 and S6), which is consistent with both species possessing a Co^{II}-(spiro^{cat-cat})-Co^{II} redox state. Two-electron oxidation of **4** through metal-based process III' affords a golden yellow solution attributed to a Co^{III}-(spiro^{SQ-SQ})-Co^{III} species. This is in contrast to the red-color associated with complex **6**, with nominally the same charge distribution, which likely arises from differences in ligand field strength between the ancillary ligands tpa and Me₃tpa. In any case, after two-electron oxidation of **4**, the electronic absorption spectrum no longer displays the pattern of bands between 500 and 750 nm assigned as MLCT bands from cobalt(II) to the singly occupied π^* orbital of the semiquinonate form of the spiro ligand, consistent with oxidation of both metal centers to cobalt(III).

Magnetochemistry. Variable-temperature magnetic susceptibility data for compounds **1a**, **3a**, **4a**, and **6a** are plotted as

$\chi_M T$ versus T in Figure 6, where χ_M is the molar magnetic susceptibility per dinuclear unit. The $\chi_M T$ vs T data for

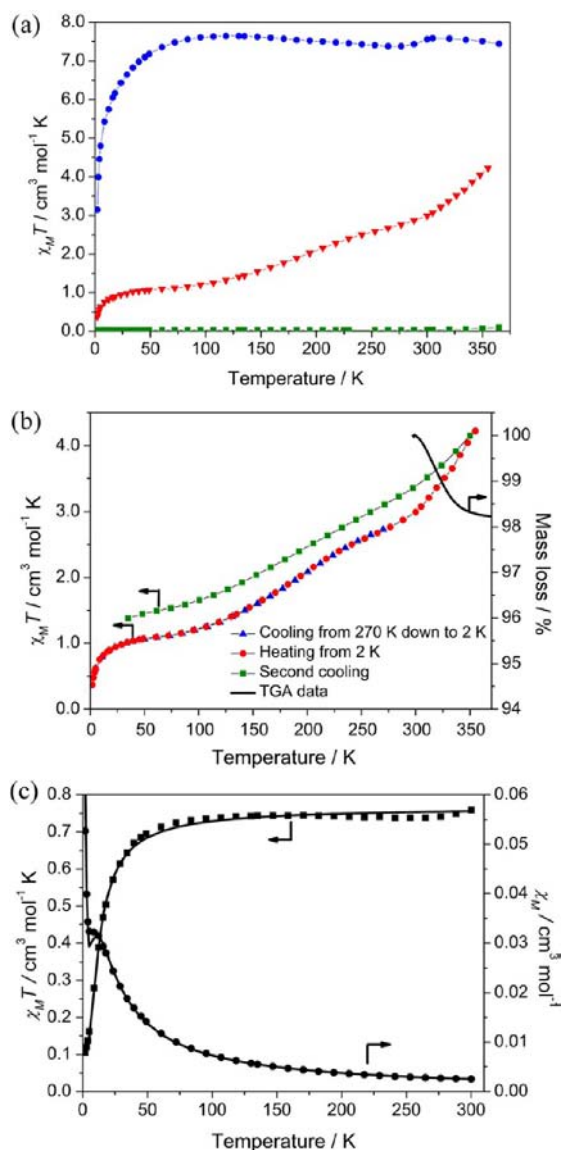


Figure 6. Variable temperature magnetic susceptibility data for (a) **1a** (green square), **3a** (red triangle) and **4a** (blue circle); (b) **3a** upon thermal cycling with the thermogravimetric analysis data superimposed; and (c) **6a** χ_M (black circle) and $\chi_M T$ (black square), with the solid line representing the best fit to the data as indicated in the text.

compound **1a** (Figure 6a) display little variation in the range 2–360 K, from 0.02 to 0.10 $\text{cm}^3 \text{mol}^{-1} \text{K}$ consistent with a diamagnetic LS-Co^{III}-(spiro^{cat-cat})-LS-Co^{III} species. The data for compound **4a** (Figure 6a) exhibit an almost constant $\chi_M T$ value of ca. 7.4 $\text{cm}^3 \text{mol}^{-1} \text{K}$ between 60 and 360 K, with a gradual decrease in $\chi_M T$ to ca. 3.2 $\text{cm}^3 \text{mol}^{-1} \text{K}$ at 2 K due to depopulation of the HS-cobalt(II) energy levels split by spin-orbit coupling. The 360 K $\chi_M T$ value is comparable to twice the value of 3.3–3.8 $\text{cm}^3 \text{mol}^{-1} \text{K}$ that has been observed for mononuclear HS-Co^{II}-SQ complexes^{28,52} and is consistent with two noninteracting semiquinonate radical ligands ($S = 1/2$, $g = 2.0$) and two HS-cobalt(II) ions ($S = 3/2$, $^4T_{1g}$ state with significant spin-orbit coupling). The data in the range 2–360

K therefore indicate a temperature-invariant HS-Co^{II}-(spiro^{SQ-SQ})-HS-Co^{II} electronic state. A small dip in $\chi_M T$ is evident around 270 K and may be assigned to a reversible structural rearrangement of the ligands, which causes a modification in the degree of orbital momentum quenching, as has been observed previously for [Co(NO₃)₂(L)] ($L = 2,6$ -di(pyrazol-1-yl)pyrazine).⁵³ Thus the powder magnetic susceptibility data are consistent with complexes **1** and **4** possessing temperature-invariant LS-Co^{III}-(spiro^{cat-cat})-LS-Co^{III} and HS-Co^{II}-(spiro^{SQ-SQ})-HS-Co^{II} electronic states, respectively, between 2 and 360 K.

Variable-temperature $\chi_M T$ data for compound **3a** indicate very interesting temperature-dependent behavior for complex **3** (Figure 6a,b). A two-step transition is evident between 2 and 355 K, with two distinct regions of change in the ranges of 100–300 and 300–355 K. These are assigned to a two-step VT transition, with both steps incomplete. Upon heating the sample from 2 K, the onset of the first step of the VT transition occurs at ca. 100 K. Below this temperature, the plateau $\chi_M T$ value of 1.1 $\text{cm}^3 \text{mol}^{-1} \text{K}$ in the range 50–100 K indicates a trapped fraction of HS-Co^{II}-SQ, amounting to ~15% of the cobalt-dioxolene “half-molecules” overall. An alternative interpretation of this plateau as due to ferromagnetic coupling between a semiquinonate radical and a LS-cobalt(II) ($S = 1/2$) center in a LS-Co^{II}-(spiro^{SQ-cat})-Co^{III}, as occurs for [Co(L-N₄tBu₂)(dbsq)]⁺ (L-N₄tBu₂ = di-*tert*-butyl derivative of 2,11-diaza[3.3](2,6)pyridinophane and dbsq⁻ = 3,5-di-*tert*-butylsemiquinone), was considered⁵⁴ but is not consistent with the X-ray absorption spectroscopy (XAS) data (see X-ray Absorption Spectroscopy section). In addition, trapped fractions of HS-Co^{II}-SQ at low temperature are evident in the magnetic susceptibility data of other VT cobalt-dioxolene complexes.³³ As the temperature is increased from 100 to 300 K, the first step of the VT transition occurs, with $\chi_M T$ increasing to a value of ca. 3.0 at 300 K, consistent with ca. 40% HS-Co^{II}-SQ. The $\chi_M T$ profile between 2 and 300 K is obtained reversibly, with no thermal hysteresis. Above 300 K, the $\chi_M T$ curve shows a steeper increase, which is assigned to the beginning of the second step of the VT transition. This step is incomplete at 355 K, with the $\chi_M T$ value of 4.2 $\text{cm}^3 \text{mol}^{-1} \text{K}$ indicating a molar fraction of about 60% HS-Co^{II}-SQ. In contrast to the first step, after heating the sample to 355 K and remeasuring the susceptibility upon cooling, the same profile is not obtained. Thermogravimetric analysis suggests that this is due to an irreversible solvent loss above 300 K, associated with the VT transition (Figure 5b). Similar behavior has been found previously for other Co VT complexes and confirms the solvation dependence of thermal VT transitions.^{23,31}

The magnetic susceptibility data for the oxidized compound **6a** (Figure 6c) display an essentially temperature-independent $\chi_M T$ value of 0.74 $\text{cm}^3 \text{mol}^{-1} \text{K}$ in the temperature range 100–300 K, with a continuous decrease to a value of 0.11 $\text{cm}^3 \text{mol}^{-1} \text{K}$ at 2 K. These data are consistent with temperature-invariant LS-Co^{III}-(spiro^{SQ-SQ})-LS-Co^{III} redox distribution for **6** in this temperature range, with a small antiferromagnetic exchange coupling between the two semiquinonate radicals across the spirocyclic carbon, affording a diamagnetic ground state. The LS-cobalt(III) centers are diamagnetic and do not contribute. The experimental data in the range 2–290 K have been least-squares fitted to the simple isotropic Heisenberg exchange Hamiltonian $\hat{H}_{\text{ex}} = -2J(\mathbf{S}_1 \cdot \mathbf{S}_2)$, where J is the exchange interaction between the two ($S = 1/2$) semiquinonate spin centers and \mathbf{S}_i are the corresponding spin operators. An

excellent fit (solid line in Figure 6c) was obtained with $J = -8.01(3) \text{ cm}^{-1}$, $g = 2.02(1)$, and $\rho = 16.0(4) \%$, where ρ corresponds to residual paramagnetism observed below 10 K due to the presence of an uncoupled $S = 1/2$ species. This species is also evident in the solution EPR spectrum of compound **6a** (see EPR Spectroscopy section) and is interpreted as a minor fraction of a species with an uncoupled semiquinonate radical. The g -value is consistent with an organic radical and the coupling constant of -8 cm^{-1} determined for the major fraction of **6** is consistent with the weak antiferromagnetic coupling reported for a nonstructurally characterized species believed to be $[\text{Co}^{\text{III}}_2(\text{spiro}^{\text{SQ-SQ}})(\text{cth})_2]^{4+}$. An antiferromagnetic exchange coupling of similar magnitude has also been reported for a spiroconjugated nitronyl nitroxide biradical.³⁰

Photomagnetic Measurements. The VT transition in cobalt-dioxolene complexes can often be induced using a light stimulus.^{4,10} At low temperatures, excitation of the LMCT band of a LS-Co^{III}-cat tautomer generally affords a LMCT excited state, which relaxes to a transient metastable HS-Co^{II}-SQ tautomer. Photoirradiation of solid compound **3a** at 10 K, with light of wavelengths 534, 658, and 904 nm, results in an increase in $\chi_M T$ from 0.84 to $1.5 \text{ cm}^3 \text{ mol}^{-1} \text{ K}$ (Figure 7a), indicative of a partial VT transition from LS-Co^{III}-(spiro^{cat-cat})-LS-Co^{III} to HS-Co^{II}-(spiro^{SQ-cat})-LS-Co^{III}. The percentage of photoconversion for the three wavelengths is in the range 15–

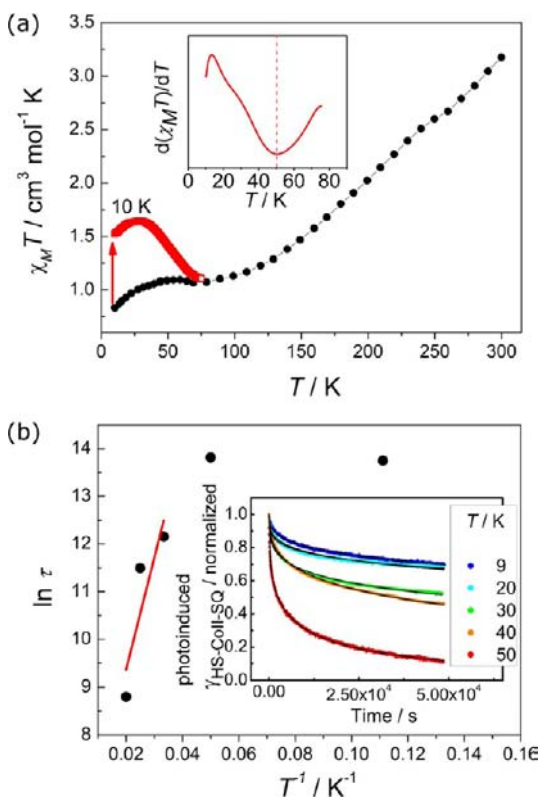


Figure 7. (a) Temperature dependence of $\chi_M T$ of compound **3a**, before (black circles) and after (red squares) 904 nm irradiation at 10 K, showing the LIESST effect. The inset shows the corresponding derivative curve, highlighting the T_{LIESST} value. (b) Arrhenius plot; pointing out the different relaxation mechanisms, along with the line of best fit, calculated as described in the text. Inset: Isothermal decays measured at different temperatures after reaching the photostationary state at 10 K, including lines of best fit as described in the text.

20% of the overall molecular Co content. On warming after 10 K irradiation, the curve collapses back to the pure (non-irradiated) one at ca. 75 K. The extrapolated T_{LIESST} parameter is found to be 52 K, suggesting the presence of a thermal activation barrier to the relaxation of similar magnitude to those reported in literature.⁹

In order to investigate the relaxation features of the photoinduced state of **3a**, isothermal relaxation profiles from the photoinduced HS-Co^{II}-(spiro^{SQ-cat})-LS-Co^{III} tautomer to the LS-Co^{III}-(spiro^{cat-cat})-LS-Co^{III} one were monitored by time-dependent magnetic susceptibility measurements at five temperatures (Figure 7b, inset). These data have been fitted using a stretched exponential model usually employed to characterize the dynamics of relaxation of metastable states with time-evolving relaxation energy barrier ($\gamma(t) = \gamma(0) \exp(-(t/\tau)^\beta)$, where t stands for measurement time, τ for the relaxation time of the system, and β is a phenomenological parameter accounting for deviation from monoexponential decay).²¹ Attempts to fit the decay profiles with a linear combination of two different monoexponential decays failed. The extracted relaxation times at different temperatures are reported as $\ln(\tau)$ versus $1/T$ (Figure 7b). This plot reveals that the relaxation rate does not follow a simple Arrhenius law as expected for a single thermally activated process. Rather, two distinct relaxation regimes are observed: a lower temperature one which is essentially temperature independent, featuring a relaxation time of about $1 \mu\text{s}$, and a higher temperature one ($T > 20 \text{ K}$) that can be tentatively fitted to an Arrhenius expression ($\tau = \tau_0 \exp(E_a/k_B T)$, where τ_0 is the pre-exponential factor and E_a is the activation energy), with best fit values of $E_a = 1.6(8) \times 10^2 \text{ cm}^{-1}$ and τ_0 of the order of 10^2 s for $T > 20 \text{ K}$. These results are consistent with the behavior observed for a number of other VT cobalt-dioxolene complexes and interpreted in terms of a phonon-assisted tunnelling mechanism in the lower temperature range and a thermally driven relaxation mechanism at higher temperatures.⁹ The value of the energy barrier to the thermally activated relaxation process may still be influenced by the presence of a tunneling mechanism to the relaxation still present at 50 K. Higher temperature measurements would be required to better estimate this value, which are not accessible with standard magnetometric techniques.

X-ray Absorption Spectroscopy. Synchrotron XAS has proved to be very useful for probing the redox and spin state of cobalt centers, making use of both the Co K- and L-edges.^{55–57} The technique is complementary to magnetic measurements for VT cobalt complexes as it essentially allows focusing on changes at the metal center in isolation from the ligands. In fact, in the process of using XAS to probe the light-induced VT transition in $[\text{Co}(3,5\text{-dbdiox})(\text{Me}_2\text{tpa})](\text{PF}_6)\cdot\text{toluene}$, Dei and co-workers found that the soft X-rays themselves could induce the VT transition, without irradiation with visible light.¹² Although the mechanism of the X-ray induced VT transition is not certain, it has been attributed to the production by inelastic scattering of secondary electrons with energy in the range of the LMCT transition that is used to stimulate the light-induced VT transition. Variable-temperature (16–298 K) Co K-edge XAS data were collected on compounds **1a–4a**, and the pre-edge, XANES and EXAFS data analyzed.

Variable-temperature Co K-edge XAS studies afforded temperature-independent spectra between 16 and 298 K for **1a**, **2a** and **4a** (Figures 8 and S7–S9; Table 4). Edge peak energies of $7729.3(\pm 0.1) \text{ eV}$ and pre-edge peak energies of

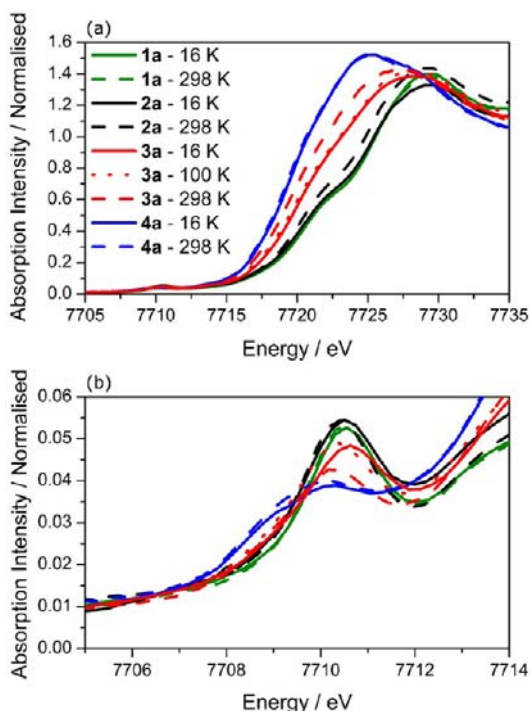


Figure 8. (a) Temperature-dependent Co K-edge XANES spectra for complexes **1a** (green), **2a** (black), **3a** (red), and **4a** (blue) collected at 16 (solid), 100 (dotted), and 298 K (dashed) and (b) shows the pre-edge region.

7710.5(± 0.1) eV are consistent with the assignment of LS-Co^{III} for both **1** and **2**, while an edge peak energy of 7725.0 eV and structures at 7708.8 and 7710.3 for the pre-edge peak confirm the assignment of **4** as HS-Co^{II}. Fitting of the Co K-edge EXAFS data (Figures S7–S8; Table 4) for compounds **1a** and **2a** at 16 and 298 K affords six Co–N/O bonds with an average bond length of 1.90 Å, while data for compound **4a** at 16, 130, and 298 K fit to four bonds at 2.06 Å and two bonds at 2.18 Å (Figure S9; Table 4). The EXAFS data for compounds **1a** and **4a** are in accord with the bond lengths determined from single crystal X-ray diffraction of compounds **1b** and **4b** at 130 K, indicating that the change of counteranion does not affect the charge distribution, which is temperature independent between 16 and 300 K.

Additional evidence for the VT nature of the low-temperature transition of compound **3a** comes from variable temperature Co K-edge XAS data. These exhibit significant temperature dependence in the range from 16 to 298 K, in contrast to the temperature-independent behavior observed for compounds **1a**, **2a**, and **4a**. The XANES, pre-edge, and EXAFS data indicate a continuous decrease in the amount of LS-cobalt(III) and a concomitant increase in the amount of HS-cobalt(II) as the sample is heated from 100 to 298 K, consistent with the first step of the VT transition evident in the magnetic susceptibility data. In the temperature range 100–298 K the XANES spectra (Figure 8) show an edge shift from 7728.4 to 7727.2 eV, while ligand-field modeling of the pre-edge data reveals the expected increase and decrease in the intensity of transitions to t_{2g} and e_g orbitals, respectively (Figure S15; Table S2). Fits of the EXAFS data (Figures S9–S14; Table 4) indicate a continuous increase in the average Co–N/O bond length from 1.97 Å at 100 K to 2.05 Å at 300 K. The average coordination environment in the dinuclear complex is best

modeled as ca. three Co–N/O bonds at 1.91 Å, two bonds at 2.07 Å, and one bond at 2.19 Å at 100 K and two Co–N/O bonds at 1.91 Å, three bonds at 2.07 Å, and one bond at 2.19 Å at 298 K. Interestingly the EXAFS, XANES, and pre-edge data below 100 K (Figures 8, S9, S14, S15; Table 4) all show some evidence of additional HS-cobalt(II), most prominent at the lowest temperature measured (16 K). This may be due to a combination of the trapped fraction of HS-Co(II)-SQ observed by magnetic susceptibility and the product of a VT transition induced by the synchrotron X-ray beam at the low temperature, as reported for [Co(3,5-dbdiox)(Me₂tpa)](PF₆)-toluene.¹² Unfortunately, instrumental limitations have prevented exploration of the second step of the VT transition of **3a** by XAS measurements above room temperature.

EPR Spectroscopy. In order to further probe the charge distribution of the one- and two-electron oxidized complexes **5** and **6**, EPR spectra have been measured for compounds **5a** and **6a** in solution. At room temperature both the X-band (9.5 GHz) and the S-band (3.8 GHz) spectra of the Co^{III}-(spiro^{SQ-cat})-Co^{III} complex **5** display a 15-line multiplet centered at $g = 2.0018$, with a separation of 4.2 G (Figure 9, left). The 15-line multiplet can be attributed to a delocalization of the unpaired electron across both halves of the spiro ligand through the spirocyclic carbon, with 15 lines due to hyperfine coupling to two equivalent ⁵⁹Co ($I = 7/2$) nuclei. It is however apparent that the relative intensities of the multiplet deviate significantly from the expected binomial distribution. To investigate this point further, we measured the temperature dependence of the X-band spectrum at variable temperatures in different solvent mixtures (Figures 9b and S16).

On decreasing temperature, line broadening and intensity loss are observed for even lines, while odd lines maintain intensity and line width until, below 220 K, the spectral pattern consists of eight lines with 8.4 G line–line separation. This behavior is typical of the so-called “alternate line width effect”, which is often revealed as alternating amplitudes of consecutive lines and implies that the radical is involved in a dynamic molecular context.⁵⁸ It was first reported in the 1960s for nitro-substituted benzene anions⁵⁹ and dihydroxydurene cation,⁶⁰ and later for transition metal based systems,^{61,23} and is usually interpreted using the model developed by Fraenkel and Freed as resulting from isotropic modulation of hyperfine coupling.⁶³ In this framework, if we assume that the time-average of the hyperfine interaction is the same for the two ⁵⁹Co nuclei, while their instantaneous values are not, the reciprocal of the transverse relaxation time $[T_{2,k}^M]^{-1}$, which determines the width of the k -th line, is given by

$$[T_{2,k}^M]^{-1} = j_{11}M^2 + 2(j_{12} - j_{11})m_1m_2 \quad (5)$$

where m_1 and m_2 are the I_z component of each ⁵⁹Co nuclei, $M = m_1 + m_2$ and j_{ij} are the spectral densities due to the modulation of hyperfine interactions produced by molecular internal motion. When the hyperfine modulation is in-phase correlated (i.e., $j_{12} = j_{11}$), the line width of all the lines depends on M^2 while, when there is an out-of phase correlation (i.e., $j_{12} = -j_{11}$), the width of the lines with even M and $m_1 \neq m_2$ depends on j_{11} . Since this value may be large, the apparent intensity of these lines is decreased compared to the expected binomial distribution.

In the present case, this is equivalent to the assumption that the radical can exist in two degenerate states, in which the unpaired electron is localized either on one or the other cobalt-

Table 4. Co–O/N Fitted Bond Distances and Occupancies As Determined by Single-Scattering EXAFS Analysis of Compounds 1a–4a^a

compound	T [K]	coordination no. (N)	bond length [R, Å]	Debye–Waller factor [σ^2 , Å ²]	$-\Delta E_0$ [eV]	fit error [%]
1a	16	6	1.910(1)	0.0031(1)	9.3(3)	
	298	6	1.911(2)	0.0041(1)	9.0(4)	
2a	16	6	1.917(2)	0.004(1)	9.8(4)	
	298	6	1.915(2)	0.0045(1)	10.1(4)	
3a	16	2.3(1)	1.91	0.0046(6)	9.7(2)	33.3
		2.7(1)	2.07	0.0072(5)		
		1.1(1)	2.19	0.007(1)		
	50	2.9(1)	1.91	0.0040(4)	9.9(2)	31.5
		2.1(1)	2.07	0.0044(6)		
		1.0(1)	2.19	0.007(2)		
	100	3.2(1)	1.91	0.0039(4)	9.5(2)	32.3
		1.8(2)	2.07	0.0036(7)		
		1.2(2)	2.19	0.008(1)		
	150	2.96(1)	1.91	0.0041(4)	9.8(2)	32.0
		2.04(1)	2.07	0.0052(7)		
		0.96(1)	2.19	0.009(2)		
	200	2.8(1)	1.91	0.0049(6)	10.2(2)	34.4
		2.2(1)	2.07	0.0051(6)		
		0.8(1)	2.19	0.0025(8)		
250	2.3(1)	1.91	0.0044(6)	10.1(3)	38.3	
	2.5(1)	2.07	0.0061(6)			
	1.23(1)	2.19	0.0048(8)			
298	1.78(9)	1.91	0.0047(8)	10.8(3)	37.6	
	2.85(9)	2.07	0.0063(7)			
	1.43(9)	2.19	0.007(1)			
4a	16	4	2.070(4)	0.0044(7)	12.7(4)	38.4
		2	2.191(7)	0.0019(9)		
	298	4	2.062(5)	0.0061(8)	13.3(4)	38.5
		2	2.188(9)	0.004(1)		

^aThe k -ranges used were: 1a, 1–16 Å⁻¹; 2a, 1–14 Å⁻¹; 3a and 4a, 1–12 Å⁻¹ and a scale factor (S_0^2) of 0.9 was used for all fits. $\Delta E_0 = E_0 - 7709$ (eV), where E_0 is the threshold energy. Values in parentheses are the estimated standard deviation derived from the diagonal elements of the covariance matrix and are a measure of precision. The fit-error is defined as $[\sum k^6(\chi_{\text{exp}} - \chi_{\text{calc}})^2 / \sum k^6 \chi_{\text{exp}}^2]^{1/2}$. A shell of ~ 7 C, fixed at a bond length of 2.88 Å, was included in the fits for 3a and 4a to model a peak observed in the Fourier transform for these species (Figures S9–S13). The fitted Debye–Waller values for this shell were ~ 0.02 Å² as expected due to the high disorder around this bond distance.

dioxolene moiety. The EPR spectrum actually observed depends then on the interconversion rate between the two states compared to the EPR time scale: when it is fast, the hyperfine splittings are completely averaged, and a 15-line pattern with binomial distribution intensity is expected. On the contrary in the limit of slow interconversion, an eight line pattern is expected with doubled line–line separation. The experimental EPR data, which changes from a 15-line spectrum at room temperature to an 8-line one at low temperature, independent of the mixture of solvent used, fully support this interpretation. This provides clear evidence of temperature-dependent delocalization of the unpaired electron over the two cobalt centers, which are not instantaneously equivalent even at room temperature. Since the existence of two conformations appears improbable due to the rigidity of the ligand, the electron delocalization process is likely activated by a specific vibronic mode of the molecule on increasing temperature. This interpretation is supported by the deconvolution of the temperature-dependent spectra as linear combination of limit spectra at 280 and 215 K. This yields a sigmoidal transition curve centered at 242 K, i.e., in the same region of the plateau observed for the two-step VT transition of 3a in solution (Figure 3c), suggesting it plays a key role in the modulation of

the enthalpic contributions related to the two different cobalt-dioxolene centers.

The temperature dependence of the X-band EPR spectrum of compound 6a was measured in CH₃CN:CH₂Cl₂ solution (Figure 10). At low temperature, a half-field transition is clearly observed which remains visible up to 50 K, confirming the existence of a sizable exchange coupling between the two semiquinone moieties, giving rise to a diamagnetic singlet and an EPR-active triplet, in agreement with solid-state magnetic data. The observation of a half-field transition further indicates that the excited $S = 1$ state is characterized by a zero-field splitting interaction parameter $D \neq 0$, a point which is confirmed by inspection of the $g = 2.00$ region, with broad and structured lines extending over 40 mT. These features could be satisfactorily simulated⁶⁴ (Figure 10, dashed lines) using the spin Hamiltonian $\hat{H} = \beta \hat{S} \cdot \mathbf{g} \cdot \mathbf{B} + D(\hat{S}_z^2 - S(S+1)/3) + E(\hat{S}_x^2 - \hat{S}_y^2)$ with the following best fit parameters: $g_x = 2.0008 \pm 0.0002$, $g_y = 2.0018 \pm 0.0002$, $g_z = 2.0028 \pm 0.0002$, $D = 0.0108 \pm 0.00002$ cm⁻¹, $E = 0.0009 \pm 0.00005$ cm⁻¹, which are in the expected range for exchange-coupled bis(semiquinone) diradical.⁶⁵ Superimposed on this is a narrow eight line hyperfine pattern, which we attribute to the paramagnetic impurity that is also evident from solid state magnetic measurement. On increasing temperature, the lines which are attributed to the

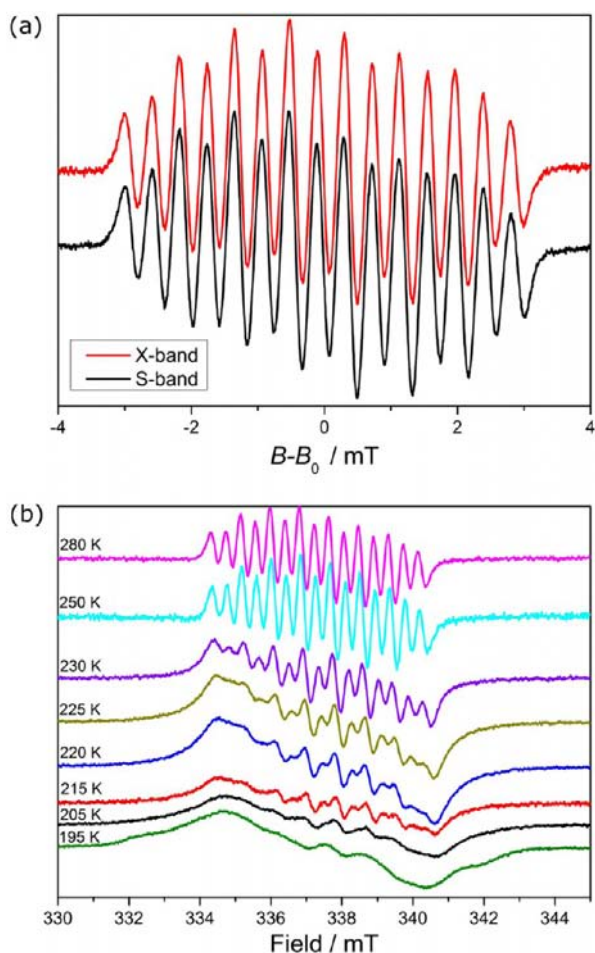


Figure 9. (a) EPR spectra of a 1:1 $\text{CH}_2\text{Cl}_2/\text{CH}_3\text{CN}$ solution of compounds **5a** at 298 K at X- and S-bands. To facilitate comparison between the two frequencies, the field has been rescaled to B_0 (i.e., the resonance field for the free electron). (b) Temperature dependence of the X-band EPR spectrum of a CH_3CN solution of compound **5a**.

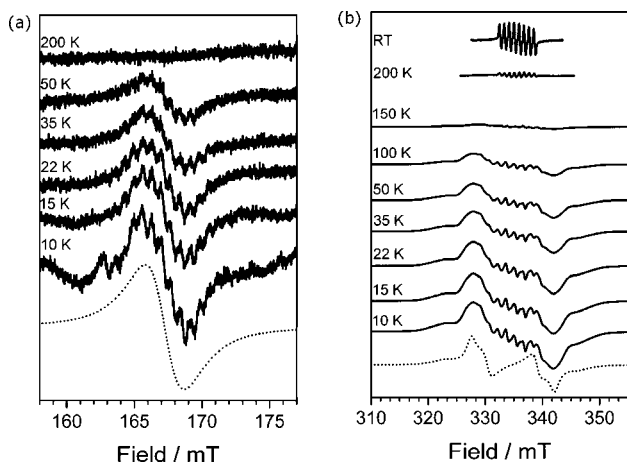


Figure 10. Temperature dependence of the X-band spectrum of **6a** recorded in a $\text{CH}_3\text{CN}:\text{CH}_2\text{Cl}_2$ (1:1) solution; (left) $\Delta M = \pm 2$ region, (right) $g = 2.00$ region. Dotted lines are the spectra simulated using the parameters reported in the text.

triplet broaden, and the superimposed hyperfine structure changes shape, so that above the melting temperature only an eight line pattern characteristic of a single unpaired electron

delocalized on a single cobalt center is observed. These results confirm those of the magnetic measurements about the exchange interaction and formation of a triplet state and suggest that at room temperature, the spectrum of **6a** is not observed due to the broadening that is often apparent for exchange-coupled diradicals.⁶⁶

CONCLUDING REMARKS

As was the case for the family of mononuclear complexes $[\text{Co}(3,5\text{-dbdiox})(\text{Me}_n\text{tpa})]^+$, derivatization of the ancillary Me_ntpa ligands has allowed tuning of the charge distribution in the family of dinuclear $[\text{Co}_2(\text{spiro})(\text{Me}_n\text{tpa})_2]^{2+}$ ($n = 0\text{--}3$) complexes, which were synthesized with the aim of finding a two-step VT transition. The two redox forms $\text{Co}^{\text{III}}(\text{spiro}^{\text{cat-cat}})\text{-Co}^{\text{III}}$ and $\text{Co}^{\text{II}}(\text{spiro}^{\text{SQ-SQ}})\text{-Co}^{\text{II}}$ have proved accessible by these means, as demonstrated by comprehensive studies in both the solid state and solution. The temperature-independent redox isomer $\text{Co}^{\text{III}}(\text{spiro}^{\text{cat-cat}})\text{-Co}^{\text{III}}$ is observed for the complexes $[\text{Co}_2(\text{spiro})(\text{Me}_n\text{tpa})_2]^{2+}$ ($n = 0$ and 1) in both the solid and solution states, while $[\text{Co}_2(\text{spiro})(\text{Me}_3\text{tpa})_2]^{2+}$ displays the $\text{Co}^{\text{II}}(\text{spiro}^{\text{SQ-SQ}})\text{-Co}^{\text{II}}$ charge distribution in both solid and solution. The charge distribution in the remaining family member, $[\text{Co}_2(\text{spiro})(\text{Me}_2\text{tpa})_2]^{2+}$, depends on both temperature and phase. At room temperature, solution electrochemical and electronic absorption studies are consistent with the existence of the $\text{Co}^{\text{II}}(\text{spiro}^{\text{SQ-SQ}})\text{-Co}^{\text{II}}$ redox isomer, while in the solid state, infrared, and X-ray absorption spectra and magnetic susceptibility data suggest the presence of a mixture of cobalt(II)/cobalt(III) and catecholate/semiquinonate. Investigation of the temperature dependence of the magnetic susceptibility data and X-ray absorption spectra for this complex in the solid state and of the electronic spectra in solution reveals that the charge distribution changes with temperature due to the occurrence of a VT transition. For the mononuclear $[\text{Co}(3,5\text{-dbdiox})(\text{Me}_n\text{tpa})]^+$ complexes, it is the Me_2tpa species that has the ligand and metal-based orbitals sufficiently close in energy to display a VT transition in the accessible 2–300 K temperature range, and it is again this ancillary ligand that gives rise to VT behavior in the dinuclear complex. Indeed the target two-step VT transition is evident for $[\text{Co}_2(\text{spiro})(\text{Me}_2\text{tpa})_2]^{2+}$ both in the solid and solution states, with sequential VT processes taking place separately at each half of the molecule from the low temperature $\text{LS-Co}^{\text{III}}(\text{spiro}^{\text{cat-cat}})\text{-LS-Co}^{\text{III}}$ tautomer to a mixed $\text{HS-Co}^{\text{II}}(\text{spiro}^{\text{SQ-cat}})\text{-LS-Co}^{\text{III}}$ species and finally to the $\text{HS-Co}^{\text{II}}(\text{spiro}^{\text{SQ-SQ}})\text{-HS-Co}^{\text{II}}$ one. This provides clear evidence of the molecular origin of the two-step VT transition in solution, which is reported for the first time in this study and allows an estimate of the relevant thermodynamic parameters. In addition to the entropy driven thermal VT transition, the charge distribution of $[\text{Co}_2(\text{spiro})(\text{Me}_2\text{tpa})_2]^{2+}$ is sensitive to low-temperature irradiation with visible light, and possibly also with soft X-rays. Temperature-dependent relaxation profiles of the photoinduced metastable state have yielded an activation barrier to thermally induced decay, which is consistent with those obtained for previously analyzed photoswitchable cobalt-dioxolene systems.

The remarkably rich redox chemistry resulting from redox activity of both the metal centers and the bridging bis-(dioxolene) ligands has allowed the isolation of two additional redox states of the dinuclear complexes: $\text{Co}^{\text{III}}(\text{spiro}^{\text{SQ-cat}})\text{-Co}^{\text{III}}$ and $\text{Co}^{\text{III}}(\text{spiro}^{\text{SQ-SQ}})\text{-Co}^{\text{III}}$. Magnetic measurements and frozen solution EPR spectra indicate modest antiferromagnetic

exchange coupling (8 cm^{-1}) between the two semiquinonate moieties in the latter species, confirming the possibility of electronic delocalization through the spirocyclic center, linking the two cobalt-dioxolene units in the dinuclear complex. Clear evidence for such electron delocalization arises from the variable temperature EPR study of the mixed-valence $\text{Co}^{\text{III}}(\text{spiro}^{\text{SQ-cat}})\text{-Co}^{\text{III}}$ species. In this case at room temperature, the unpaired electron is delocalized across both halves of the bridging ligand through the spirocyclic carbon, while localization on a single moiety occurs upon lowering the temperature. Similar observations have been reported previously for a spiroconjugated nitronyl-nitroxide biradical and are consistent with the presence of considerable overlap between $2p$ orbitals on the carbon atoms bound directly to the spirocyclic carbon atom and with vibronic activation of the delocalization.^{30,67} Interestingly, EPR spectral deconvolution reveals that the transition from localized to delocalized unpaired electron in the singly oxidized species occurs at the same temperature at which the plateau is observed in the two-step transition for $[\text{Co}_2(\text{spiro})(\text{Me}_2\text{tpa})_2]^{2+}$, suggesting that the thermally activated vibronic coupling of the two cobalt-dioxolene moieties through the spiroconjugated bridge plays a key role in the VT transition of the $[\text{Co}_2(\text{spiro})(\text{Me}_2\text{tpa})_2]^{2+}$ complex.

The accessibility of three different electronic states in a molecule via a two-step transition has implications for molecule-based materials for electronics, display devices, and ternary computing applications. This study has demonstrated the possibility of eliciting a two-step VT transition by chemically tuning the electronic interactions within a dinuclear cobalt-dioxolene complex. Employing a concerted multi-instrumental approach, it was possible to characterize the effective role played by the spirocyclic bridge in the connection of the two centers and hence on the modulation of the thermodynamics of VT conversion. Efforts to improve temperature- and light-induced VT behavior in dinuclear cobalt bis(dioxolene) complexes through these types of chemical modification are presently underway in our laboratory.

EXPERIMENTAL SECTION

Synthesis. Unless indicated otherwise, all manipulations were performed under aerobic conditions using materials as received. The tris(2-pyridylmethyl)amine ligands $(\text{H}_3\text{tpa})(\text{ClO}_4)_3$, $(\text{H}_3\text{Metpa})(\text{ClO}_4)_3$, Me_2tpa , and Me_3tpa were synthesized by literature methods using dichloromethane that was dried over CaH_2 .^{50,68}

$[\text{Co}(\text{tpa})\text{Cl}](\text{PF}_6)$. A solution of $(\text{H}_3\text{tpa})(\text{ClO}_4)_3$ (1.00 g, 1.69 mmol) and NEt_3 (705 μL , 5.07 mmol) in methanol (5 mL) was added to a stirred solution of $\text{CoCl}_2 \cdot 6\text{H}_2\text{O}$ (0.402 g, 1.69 mmol) in methanol (2 mL), giving rise to a color change from pink to dark blue. After 30 min of refluxing, a solution of excess KPF_6 (0.46 g, 2.5 mmol) in water (4 mL) was added, and the resulting solution heated for a further 15 min. Upon cooling a mixture of green and white material precipitated, which was collected by filtration. The green precipitate was dissolved in the minimum volume of acetonitrile, and the remaining white solid was removed by filtration and discarded. The filtrate was evaporated to dryness and recrystallized from warm methanol. After 1 day of slow evaporation the product was collected as large green needles, yield 80%. An air-dried sample analyzed as unsolvated. Anal. calcd for $\text{C}_{18}\text{H}_{18}\text{N}_4\text{ClCoF}_6\text{P}$: C, 40.81; H, 3.42; N, 10.58%. Found: C, 40.84; H, 3.42; N, 10.51%. Selected IR data (cm^{-1}): 3442 (m), 2923 (w), 1611 (m), 1574 (w),

1484 (m), 1440 (m), 1384 (w), 1313 (w), 1295 (w), 1268 (w), 1163 (w), 1123 (w), 1105 (w), 1055 (w), 1026 (w), 1003 (w), 982 (w), 966 (w), 904 (w), 857 (s), 837 (s), 769 (m), 732 (w), 652 (w), 558 (m), 507 (w), 473 (w), 423 (w).

$[\text{Co}_2(\text{spiro})(\text{tpa})_2](\text{ClO}_4)_2 \cdot 6\text{H}_2\text{O}$ (**1a**). A heated solution of $(\text{H}_3\text{tpa})(\text{ClO}_4)_3$ (1.00 g, 1.69 mmol) and NEt_3 (705.3 μL , 5.07 mmol) in methanol (2 mL) was added to a solution of $\text{Co}(\text{ClO}_4)_2 \cdot 6\text{H}_2\text{O}$ (0.309 g, 0.845 mmol) in warm methanol (1 mL), affording a light brown solution. After 10 min of heating, a mixture of spiroH_4 (0.300 g, 0.881 mmol) and NEt_3 (470 μL , 3.53 mmol) in methanol (1 mL) was added dropwise. A light green precipitate started to form almost immediately. After stirring for 30 min the precipitate was isolated by filtration, washed with methanol/diethyl ether, and air-dried; yield 89%. Green hexagonal crystals were obtained by slow evaporation of an acetonitrile/toluene solution over a period of ~ 5 days or by layering an acetonitrile solution with diethyl ether. The air-dried sample appeared hygroscopic, analyzing as $[\text{Co}_2(\text{spiro})(\text{tpa})_2](\text{ClO}_4)_2 \cdot 6\text{H}_2\text{O}$. Anal. calcd for $\text{C}_{57}\text{H}_{68}\text{N}_8\text{Cl}_2\text{Co}_2\text{O}_{18}$: C, 51.02; H, 5.11; N, 8.35; Cl, 5.28%. Found: C, 50.55; H, 4.66; N, 8.19; Cl, 5.31%. Selected IR data (cm^{-1}): 3424 (s), 2938 (m), 2859 (w), 1635 (m), 1609 (m), 1575 (w), 1479 (s), 1446 (m), 1384 (w), 1357 (w), 1330 (m), 1281 (s), 1228 (w), 1201 (w), 1143 (m), 1121 (s), 1108 (s), 1091 (s), 990 (w), 941 (w), 905 (w), 883 (w), 854 (w), 822 (m), 772 (m), 731 (m), 720 (w), 664 (w), 626 (m), 602 (m), 533 (w), 506 (m), 448 (w).

$[\text{Co}_2(\text{spiro})(\text{tpa})_2](\text{PF}_6)_2 \cdot 4\text{py}$ (**1b**), Method 1. A heated solution of $(\text{H}_3\text{tpa})(\text{ClO}_4)_3$ (0.500 g, 0.845 mmol) and NEt_3 (353 μL , 2.53 mmol) in methanol (2 mL) was added to a stirred solution of $\text{Co}(\text{ClO}_4)_2 \cdot 6\text{H}_2\text{O}$ (0.309 g, 0.845 mmol) in methanol (1 mL). This was refluxed for 5 min before TBAPF_6 (1.50 g, 3.87 mmol) was added. After refluxing for 10 min, a warm solution of spiroH_4 (0.144 g, 0.422 mmol) and NEt_3 (235 μL , 1.69 mmol) methanol (2 mL) was added dropwise to give a dark green solution, which was refluxed for ~ 2 h until a light green precipitate formed. A small quantity of crystals suitable for crystallography was obtained by layering a pyridine solution under hexane for a few days and identified as $[\text{Co}_2(\text{spiro})(\text{tpa})_2](\text{PF}_6)_2 \cdot 4\text{py}$ (**1b**). A small sample for IR was obtained following recrystallization from pyridine/hexane. Selected IR data (cm^{-1}): 3424 (m), 2937 (w), 2857 (w), 1891 (w), 1610 (m), 1574 (w), 1478 (s), 1446 (m), 1403 (w), 1384 (w), 1331 (m), 1281 (s), 1228 (w), 1182 (w), 1160 (w), 1121 (m), 1092 (m), 1056 (w), 991 (w), 942 (w), 846 (s), 772 (m), 732 (w), 721 (w), 664 (w), 623 (m), 602 (w), 559 (m), 506 (w), 445 (w).

Method 2. Solid silver triflate (0.36 g, 1.41 mmol) was added to a solution of $[\text{Co}(\text{tpa})\text{Cl}](\text{PF}_6)$ (0.500, 0.943 mmol) in methanol (5 mL), and the resulting white solid (AgCl) was removed by filtration, leaving a light brown filtrate. A mixture of spiroH_4 (0.160 g, 0.472 mmol) and NEt_3 (263 μL , 1.89 mmol) in methanol (1 mL) was added to this brown solution, and any silver metal/oxide that formed was quickly removed by filtering through filter paper. After ~ 1 h a light green precipitate formed, which was removed by filtration and recrystallized by slowly diffusing hexane into a concentrated pyridine solution. Dark green rectangular prism crystals suitable for crystallography were identified as $[\text{Co}_2(\text{spiro})(\text{tpa})_2](\text{PF}_6)_2 \cdot 4\text{py}$ (**1b**). A small quantity of crystals were isolated after ~ 2 days and were washed with the minimum pyridine/hexane. Selected IR data (cm^{-1}): 3440 (m), 3109 (w), 3073 (w), 2925 (m), 2856 (m), 2025 (w), 1610 (m), 1576 (w), 1477 (s), 1441 (m), 1384 (w), 1334 (m), 1279 (s), 1224 (m), 1160 (m), 1100 (m), 1031 (m),

992 (w), 957 (w), 940 (w), 843 (s), 773 (m), 733 (m), 708 (m), 664 (m), 638 (m), 623 (w), 599 (m), 558 (w), 518 (w), 506 (w), 444 (w).

$[\text{Co}_2(\text{spiro})(\text{Metpa})_2](\text{ClO}_4)_2 \cdot 4\text{H}_2\text{O}$ (**2a**). This was synthesized in a manner analogous to **1a**, with $(\text{H}_3\text{tpa})(\text{ClO}_4)_3$ replaced by $(\text{H}_3\text{Metpa})(\text{ClO}_4)_3$, and the precipitate that formed purified by dissolution in acetonitrile and precipitated with the slow addition of diethyl ether; yield 52%. The air-dried sample appeared hygroscopic, analyzing as $[\text{Co}_2(\text{spiro})(\text{Metpa})_2](\text{ClO}_4)_2 \cdot 4\text{H}_2\text{O}$. Anal. calcd for $\text{C}_{59}\text{H}_{68}\text{N}_8\text{Cl}_2\text{Co}_2\text{O}_{16}$: C, 53.12; H, 5.14; N, 8.40; Cl 5.32, %. Found: C, 53.40; H, 4.71; N, 7.85; Cl, 4.95%. Selected IR data (cm^{-1}): 3427 (m), 3076 (m), 2947 (m), 2859 (m), 2013 (w), 1610 (m), 1576 (m), 1478 (s), 1443 (m), 1384 (w), 1333 (m), 1281 (s), 1224 (w), 1158 (m), 1097 (s), 1021 (w), 995 (w), 963 (w), 942 (w), 882 (m), 854 (m), 823 (m), 773 (m), 721 (w), 664 (w), 627 (w), 600 (m), 542 (w), 447 (w).

$[\text{Co}_2(\text{spiro})(\text{Me}_2\text{tpa})_2](\text{ClO}_4)_2 \cdot 3.5\text{H}_2\text{O}$ (**3a**). Under a nitrogen atmosphere, solid Me_2tpa (0.500 g, 1.57 mmol) was added to a stirred solution of $\text{Co}(\text{ClO}_4)_2 \cdot 6\text{H}_2\text{O}$ (0.562 g, 1.54 mmol) in methanol (2 mL). After 15 min of stirring, a preformed methanol solution (3 mL) of spiro H_4 (0.272 g, 0.799 mmol) and imidazole (0.213 g, 3.13 mmol) was added dropwise forming a light brown solution. Following 30 min of stirring under nitrogen, air was bubbled through the reaction for ~1 h until a dark blue microcrystalline precipitate formed. This product was filtered and washed with a minimum of methanol/diethyl ether. Recrystallization from acetone/cyclohexane afforded dark blue needle-like crystals, which were isolated by filtration washed with a minimum mixture of acetone/diethyl ether and air dried; yield 70%. The air-dried sample appeared hygroscopic, analyzing as $[\text{Co}_2(\text{spiro})(\text{Me}_2\text{tpa})_2](\text{ClO}_4)_2 \cdot 3.5\text{H}_2\text{O}$. Anal. calcd for $\text{C}_{61}\text{H}_{71}\text{N}_8\text{Cl}_2\text{Co}_2\text{O}_{15.5}$: C, 54.15; H, 5.29; N, 8.28; Cl, 5.24%. Found: C, 53.92; H, 5.33; N, 8.27; Cl, 5.34%. Selected IR data (cm^{-1}): 3440 (m), 3074 (w), 2954 (m), 2927 (m), 2861 (w), 2011 (w), 1895 (w), 1713 (w), 1607 (s), 1578 (m), 1526 (w), 1481 (s), 1455 (s), 1387 (w), 1349 (w), 1287 (m), 1233 (w), 1165 (w), 1097 (s), 1013 (m), 973 (w), 913 (w), 887 (w), 854 (w), 788 (m), 722 (w), 673 (w), 624 (m), 539 (w), 513 (w), 418 (w).

$[\text{Co}_2(\text{spiro})(\text{Me}_3\text{tpa})_2](\text{ClO}_4)_2 \cdot 2\text{H}_2\text{O}$ (**4a**). Solid Me_3tpa (0.500 g, 1.50 mmol) was added to a solution of $\text{Co}(\text{ClO}_4)_2 \cdot 6\text{H}_2\text{O}$ (0.550, 1.50 mmol) in methanol (2 mL) under a nitrogen atmosphere. After stirring for 15 min, a solution of spiro H_4 (0.256 g, 0.752 mmol) and NEt_3 (418.4 μL , 3.01 mmol) in methanol (1 mL) was added dropwise. After stirring for 30 min the nitrogen atmosphere was removed, and air was bubbled through the solution. A dark blue precipitate formed, which was isolated by filtration and washed with the minimum methanol. This solid was recrystallized by layering a concentrated acetonitrile solution with diethyl ether to give blue rectangular plates, which were isolated by filtration, washed with an acetonitrile/diethyl ether mixture and air dried; yield 92%. The air-dried sample appeared hygroscopic, analyzing as $[\text{Co}_2(\text{spiro})(\text{Me}_3\text{tpa})_2](\text{ClO}_4)_2 \cdot 2\text{H}_2\text{O}$. Anal. calcd for $\text{C}_{63}\text{H}_{72}\text{N}_8\text{Cl}_2\text{Co}_2\text{O}_{14}$: C, 55.88; H, 5.36; N, 8.28; Cl, 5.24%. Found: C, 56.02; H, 5.01; N, 8.48; Cl, 5.36%. Selected IR data (cm^{-1}): 3432 (m), 3075 (w), 2957 (m), 2926 (m), 2864 (w), 2009 (w), 1606 (s), 1579 (m), 1526 (m), 1486 (s), 1454 (s), 1387 (m), 1352 (m), 1326 (m), 1298 (w), 1266 (m), 1224 (w), 1192 (w), 1167 (m), 1097 (s), 1010 (m), 972 (w), 944 (w), 916 (w), 874 (w), 853 (w), 790 (m), 749 (w), 720 (w), 670 (w), 623 (s), 558 (w), 538 (w), 465 (w).

$[\text{Co}_2(\text{spiro})(\text{Me}_3\text{tpa})_2](\text{CoCl}_4) \cdot 7\text{MeOH}$ (**4b**). This complex was synthesized following the procedure described above for $[\text{Co}_2(\text{spiro})(\text{Me}_3\text{tpa})_2](\text{ClO}_4)_2$, with $\text{CoCl}_2 \cdot 6\text{H}_2\text{O}$ replaced by $\text{Co}(\text{ClO}_4)_2 \cdot 6\text{H}_2\text{O}$. Immediately prior to the onset of precipitation, a sample of the reaction solution was removed and layered under diethyl ether, giving a small quantity of dark blue rectangular plate-shaped crystals within a few hours. The sample was crystallographically identified as $[\text{Co}_2(\text{spiro})(\text{Me}_3\text{tpa})_2](\text{CoCl}_4) \cdot 7\text{MeOH}$. These crystals were obtained in a very small yield preventing any further analysis.

$[\text{Co}_2(\text{spiro})(\text{tpa})_2](\text{PF}_6)_3$ (**5a**), Method 1. A solution of ferrocium hexafluorophosphate (0.059 g, 0.18 mmol) in acetonitrile (1 mL) was added to a warm solution of $[\text{Co}_2(\text{spiro})(\text{tpa})_2](\text{PF}_6)_2$ (0.20 g, 0.16 mmol) in the minimum acetonitrile. The resulting green solution immediately changed to dark brown and was filtered through Celite and gently warmed until the volume was reduced by a half. While warming, ethyl acetate was added to precipitate the crude product. This was then filtered and washed with warm ethyl acetate followed by diethyl ether. The crude material was purified by dissolution in acetone and precipitation with diethyl ether. The resulting brown powder was then filtered and washed with ethyl acetate and diethyl ether; yield 31%. The air-dried sample analyzed as solvent-free. Anal. calcd for $\text{C}_{57}\text{H}_{56}\text{N}_8\text{P}_3\text{F}_{18}\text{Co}_2\text{O}_4$: C, 46.58; H, 3.84; N, 7.62; P, 6.32%. Found: C, 46.94; H, 4.07; N, 7.42; P, 6.15%. Selected IR data (cm^{-1}): 3431 (m), 3113 (w), 2956 (w), 2928 (w), 2862 (w), 1655 (w), 1634 (w), 1611 (m), 1574 (w), 1531 (w), 1528 (w), 1480 (m), 1468 (m), 1448 (w), 1385 (w), 1336 (w), 1282 (m), 1231 (w), 1121 (m), 1108 (m), 1040 (w), 1028 (w), 942 (w), 845 (s), 774 (w), 732 (w), 663 (w), 626 (w), 558 (m), 506 (w), 446 (w).

Method 2. A mixture of **1b** (0.082 g, 0.062 mmol) and **6a** (0.10 g, 0.062) in acetonitrile (5 mL) was stirred for 20 min to give a brown solution, which was then filtered through Celite to remove any undissolved reactants. Ethyl acetate was slowly added to precipitate a brown powder. This powder was then redissolved in acetonitrile and layered with diethyl ether for about 2 days in the dark to afford the product as a dark brown powder, yield 77%. The air-dried sample appeared hygroscopic, analyzing as $[\text{Co}_2(\text{spiro})(\text{tpa})_2](\text{PF}_6)_3 \cdot 2\text{H}_2\text{O}$. Anal. calcd for $\text{C}_{57}\text{H}_{60}\text{N}_8\text{P}_3\text{F}_{18}\text{Co}_2\text{O}_6$: C, 45.46; H, 4.02; N, 7.44; P, 6.17%. Found: C, 45.3; H, 4.04; N, 7.41; P, 5.86%. Selected IR data (cm^{-1}): 3441 (w), 3117 (w), 2961 (w), 2926 (w), 2856 (w), 1612 (w), 1469 (m), 1389 (w), 1337 (w), 1281 (w), 1262 (w), 1232 (w), 1163 (w), 1099 (w), 1061 (w), 1040 (w), 1026 (w), 941 (w), 842 (s), 771 (w), 734 (w), 663 (w), 624 (w), 558 (m), 506 (w), 446 (w).

$[\text{Co}_2(\text{spiro})(\text{tpa})_2](\text{PF}_6)_4 \cdot 2\text{H}_2\text{O}$ (**6a**) and $[\text{Co}_2(\text{spiro})(\text{tpa})_2](\text{PF}_6)_4 \cdot 4\text{Me}_2\text{CO}$ (**6b**). To a suspension of **1b** (0.45 g, 0.34 mmol) in methanol was added silver triflate (0.350 g, 1.35 mmol). Immediately the solution turned from dark green to an intense red. After 5 min of stirring the solution was filtered through Celite to remove the silver solid that formed. A methanol (3 mL) solution of NH_4PF_6 (0.28 g, 1.70 mmol) was added dropwise, affording a mixture of red solid and yellow/orange solids. Following 15 min of stirring the precipitate was isolated by filtration and washed with the minimum of methanol. The crude precipitate was dissolved in acetone, and the residual yellow/orange precipitate was removed by filtration. Layering the acetone solution with diethyl ether produced small red crystals, which were identified crystallographically as the acetone solvate $[\text{Co}_2(\text{spiro})(\text{tpa})_2]$

(PF₆)₄·4Me₂CO (**6b**), yield 50%. The air-dried sample loses acetone molecules of solvation and is hygroscopic, analyzing as [Co₂(spiro)(tpa)₂](PF₆)₄·2H₂O (**6a**). Anal. calcd for C₅₇H₆₀N₈P₄F₂₄Co₂O₆: C, 41.47; H, 3.66; N, 6.79; P, 7.50%. Found: C, 41.09; H, 3.41; N, 6.43; P, 7.46%. Selected IR data (cm⁻¹): 3442 (m), 3123 (w), 2959 (w), 2928 (w), 2865 (w), 1657 (w), 1638 (w), 1612 (w), 1578 (w), 1530 (w), 1479 (w), 1469 (m), 1448 (w), 1385 (w), 1336 (w), 1282 (w), 1232 (w), 1163 (w), 1121 (w), 1101 (w), 1061 (w), 941 (w), 842 (s), 773 (w), 738 (w), 663 (w), 623 (w), 558 (m), 506 (w), 448 (w).

X-ray Data Collection and Structure Solution. The crystallographic data (Table 1) for compounds **1b**, **4b**, and **6a** were collected at 130 K on an Oxford Diffraction Excalibur diffractometer using graphite monochromatic Cu-K α radiation ($\lambda = 1.54184 \text{ \AA}$). Crystals were transferred from the mother liquor to a protective oil to prevent potential solvent loss. The structures were solved using direct methods and refined using a full-matrix least-squares procedure based on F^2 using all data.¹ For **4b** the Fourier difference map indicated two large regions within the unit cell that contained highly disordered methanol molecules. It was not possible to satisfactorily model these molecules, and as a consequence the SQUEEZE routine within PLATON² was used to estimate the size of these solvent-filled regions and the electron density within them. The PLATON program generated a modified data file in which the contribution of the disordered solvent to the diffraction data was removed. The structure was refined using the modified data. Similar problems with disordered solvent and a PF₆⁻ anion were encountered with compound **6b**. Attempts to model the solvent and anion were unsuccessful, and as a result the SQUEEZE routine within PLATON was once again employed to generate a modified data file with the contribution of the disordered solvent and anion removed.

Electrochemistry and Spectroelectrochemistry. Electrochemical measurements were performed in acetonitrile at $293 \pm 2 \text{ K}$ using a standard three-electrode configuration under a flow of nitrogen gas or in a Vacuum Atmospheres glovebox connected to a BASi EC Epsilon computer-controlled electrochemical workstation or a computer-controlled eDAQ potentiostat. The three-electrode arrangement employed for cyclic voltammetric measurements consisted of 1.0 mm diameter glassy carbon (eDAQ) disk working electrode, a platinum wire counter electrode, and a reference electrode consisting of a AgCl-coated Ag wire, prepared by oxidative electrolysis of the wire in 0.1 M KCl solution, or a commercial Ag/AgCl electrode (eDAQ), separated from the analyte solution by a glass frit of low porosity containing the same solvent/supporting electrolyte mixture. For RDE voltammetry a 3 mm glassy carbon (Metrohm) working electrode was employed, connected to a Metrohm rotator. For bulk electrolysis experiments, large platinum gauze and platinum mesh baskets were used as the working and counter electrodes, respectively. The Ag/AgCl reference electrode was the same as that employed in the voltammetric studies. The progress of the electrolyses was monitored by linear sweep voltammetry using a 10 μm platinum electrode. Analyte solutions of 1 mM were prepared in acetonitrile containing 0.1 M Bu₄NPF₆ as the supporting electrolyte. All potentials reported in this paper are in volts versus the ferrocene/ferrocenium redox couple. UV-vis spectroelectrochemistry was performed *ex situ* by transferring the electrolyzed solution to a 1 cm quartz cuvette with an airtight lid and diluting to $\sim 0.13 \text{ mM}$. The experiments employed $\sim 8 \text{ mL}$ of acetonitrile solutions containing 0.1 M

[Bu₄N][PF₆] and 0.1 mM analyte. The UV-vis spectra were recorded with a Varian Cary 5000 spectrophotometer.

X-ray Absorption Spectroscopy. The cobalt K-edge X-ray absorption spectra of the complexes as pressed disks in cellulose were recorded at the XAS beamline at the Australian Synchrotron. The X-ray beam was monochromated by diffraction from a pair of Si(111) crystals. Data were collected as transmission spectra using helium-filled ion chambers at a range of temperatures as outlined below controlled by a Cryo Industries (Manchester, New Hampshire, U.S.A.) cryostat. The energy ranges used for the XAS data collection were: pre-edge region, 7510–7689 eV (10 eV steps); XANES region, 7689–8000 eV (0.25 eV steps); EXAFS region to data range indicated in Table 4 in steps of 0.035 \AA^{-1} . Energy calibration was achieved by simultaneously recording the spectrum of a Co foil in transmission downstream of the sample, with the first peak of the first derivative arbitrarily set at 7709.0 eV. Data analysis, including calibration, averaging, and background subtraction of all spectra, was undertaken using the EXAFSPAK suite of programs (G. N. George, SSRL). Subsequent scans recorded on one spatial location on the sample revealed no evidence for variation in the XANES spectra as a function of exposure.

Ligand Field Analysis. To gain an estimate of the spin state of the material from a ligand field analysis of the pre-edge XAS data, each edge was background subtracted and fit with three pseudo Voigt functions of identical line width, the fits are shown in Figure S6. Each peak was used to estimate t_{2g} (peak 1), e_g (peak 2), and an edge transition (peak 3) in each fit. Formally the transitions to the edge are more complicated than this and dominated by all relevant electron repulsion states.^{3,4} However, in this instance it represents a good estimate as the ligand field effect is large relative to the electron repulsion effects, and the compounds are close to octahedral.^{5,6}

Magnetic Susceptibility Measurements. Variable temperature magnetic susceptibility measurements without light irradiation were performed with a Quantum Design MPMS-5 susceptometer, equipped with a 5 T magnet. Data were collected on powdered, dry crystals in a gelatin capsule. Pascal's constants were used to estimate the diamagnetic correction for each complex.

Magnetic Measurements under Light Irradiation. The sample of **3a** for photomagnetic characterization was obtained by mixing $\sim 0.5 \text{ mg}$ of microcrystalline powder (the actual Co content being evaluated by scaling the magnetic moment on that of a polycrystalline heavier sample) with KBr powder and pressing into a pellet to facilitate light penetration. Irradiation experiments have been performed at different wavelengths (534, 658, and 904 nm) with the specific CW laser diode coupled to an optical fiber inserted in the sample space through a hollow sample rod and collimated on the sample by means of an aspheric lens, yielding a radiant power on the sample of about 5 mW cm^{-2} . Magnetic moments were corrected for the diamagnetic contribution of the KBr and the sample holder, independently measured in the same range of field and temperature as well as for the intrinsic diamagnetism of the sample by using appropriate Pascal constants. T_{LIESST} measurement consisted of monitoring the temperature featuring a minimum in the $d(\chi_M T)/dT$ curve, after reaching the photostationary limit, having switched the laser off at 10 K and warming the sample at a rate of 0.3 K min^{-1} .

EPR Spectroscopy. Temperature-dependent EPR studies were performed using a Bruker Elexsys E500 spectrometer equipped with a ER4131VT liquid nitrogen cryostat (Bruker)

for **5a** (130–300 K) and a ^4He continuous flow cryostat (ESR900, Oxford Instruments) for **6a**. S-band EPR spectra were obtained on a Bruker 200 D-SRC spectrometer equipped with a S-band bridge ($\nu = 2\text{--}4$ GHz) SB-1111 Jagmar (Poland)

Other Measurements. Infrared spectra were recorded on a Bruker FTIR Tensor 27 spectrometer as pressed KBr disks. Thermogravimetric analyses were performed on a Mettler Toledo thermal analyzer. Electronic absorption spectra were measured on a Varian 50 Bio UV–vis spectrophotometer. Elemental analyses were performed by the Microanalytical Unit, Research School of Chemistry, Australian National University, Australia, and by The Campbell Microanalytical Laboratory, Department of Chemistry, University of Otago, New Zealand.

■ ASSOCIATED CONTENT

■ Supporting Information

Crystallographic data (CIF), structural parameters and diagrams, infrared, electronic absorption, EPR and X-ray absorption spectra and data, and voltammograms. This material is available free of charge via the Internet at <http://pubs.acs.org>.

■ AUTHOR INFORMATION

Corresponding Author

c.boskovic@unimelb.edu.au

Present Address

∇ Department of Chemistry, College of Science & Sustainable Energy Technologies (SET) Center, King Saud University, Saudi Arabia.

Notes

The authors declare no competing financial interest.

■ ACKNOWLEDGMENTS

This research was funded by the Australian Research Council (separate Discovery Grants to C.B. and K.S.M.); G.P. and L.S. thank the European Research Council for funding through ERC-AdG MolNanoM@S. C.B. thanks Prof. N. Frank for helpful discussions. L.S. and G.P. thank Prof. A. Dei for fruitful discussions and suggestions and Dr.ssa M. C. Baratto (University Of Siena) for assistance in recording S-band spectra. Portions of this work were performed at the XAS beamline at the Australian Synchrotron.

■ REFERENCES

- (1) *Topics in Current Chemistry* Gütllich, P., Goodwin, H. A., Eds.; Springer: New York, 2004; pp 233–235, complete volumes.
- (2) Shatruk, M.; Avendano, C.; Dunbar, K. R. *Prog. Inorg. Chem.* **2009**, *56*, 155.
- (3) Newton, G. N.; Nihei, M.; Oshio, H. *Eur. J. Inorg. Chem.* **2011**, 3031.
- (4) Sato, O.; Tao, J.; Zhang, Y. *Z. Angew. Chem., Int. Ed.* **2007**, *46*, 2152.
- (5) Hendrickson, D. N.; Pierpont, C. G. *Top. Curr. Chem.* **2004**, *234*, 63.
- (6) Dei, A.; Gatteschi, D.; Sangregorio, C.; Sorace, L. *Acc. Chem. Res.* **2004**, *37*, 827.
- (7) Evangelio, E.; Ruiz-Molina, D. *Eur. J. Inorg. Chem.* **2005**, 2957.
- (8) *Spin-Crossover Materials - Properties and Applications*, Halcrow, M. A., Ed.; Wiley: Chichester, 2013.
- (9) Dei, A.; Sorace, L. *Appl. Magn. Reson.* **2010**, *38*, 139.
- (10) Sato, O.; Cui, A.; Matsuda, R.; Tao, J.; Hayami, S. *Acc. Chem. Res.* **2007**, *40*, 361.

- (11) Markevtsev, I.; Monakhov, M.; Platonov, V.; Mischenko, A.; Zvezdin, A.; Bubnov, M.; Abakumov, G.; Cherkasov, V. *J. Magn. Mag. Mater.* **2006**, *300*, e407.
- (12) Poneti, G.; Mannini, M.; Sorace, L.; Sainctavit, P.; Arrio, M. –A.; Otero, E.; Cezar, J. C.; Dei, A. *Angew. Chem., Int. Ed.* **2010**, *49*, 1954.
- (13) Balzani, V.; Venturi, M.; Credi, A. *Molecular Devices and Machines*; Wiley: Weinheim, 2003.
- (14) Simão, C.; Mas-Torrent, M.; Casado-Montenegro, J.; Oton, F.; Veciana, J.; Rovira, C. *J. Am. Chem. Soc.* **2011**, *133*, 13256.
- (15) Bousseksou, A.; Molnár, G.; Real, J. A.; Tanaka, K. *Coord. Chem. Rev.* **2007**, *251*, 1822.
- (16) Jung, O. –S. J.; Jo, D. H.; Lee, Y. –A.; Chae, H. K.; Sohn, Y. S. *Bull. Chem. Soc. Jpn.* **1995**, *69*, 2211.
- (17) Bin-Salamon, S.; Brewer, S. H.; Depperman, E. C.; Franzen, S.; Kampf, J. W.; Kirk, M. L.; Kumar, R. K.; Lappi, S.; Peariso, K.; Preuss, K. E.; Shultz, D. A. *Inorg. Chem.* **2006**, *45*, 4461.
- (18) Hearn, N. G. R.; Korčok, J. L.; Paquette, M. M.; Preuss, K. E. *Inorg. Chem.* **2006**, *45*, 8817.
- (19) Bencini, A.; Daul, C. A.; Dei, A.; Mariotti, F.; Lee, H.; Shultz, D. A.; Sorace, L. *Inorg. Chem.* **2001**, *40*, 1582.
- (20) Carbonera, C.; Dei, A.; Létard, J.-F.; Sangregorio, C.; Sorace, L. *Angew. Chem., Int. Ed.* **2004**, *43*, 3136.
- (21) Tao, J.; Maruyama, H.; Sato, O. *J. Am. Chem. Soc.* **2006**, *128*, 1790.
- (22) Dapporto, P.; Dei, A.; Poneti, G.; Sorace, L. *Chem.—Eur. J.* **2008**, *14*, 10915.
- (23) Mulyana, Y.; Poneti, G.; Moubaraki, B.; Murray, K. S.; Abrahams, B. F.; Sorace, L.; Boskovic, C. *Dalton Trans.* **2010**, *39*, 4757.
- (24) Evangelio, E.; Rodriguez-Blanco, C.; Coppel, Y.; Hendrickson, D. N.; Sutter, J. P.; Campo, J.; Ruiz-Molina, D. *Solid State Sci.* **2009**, *11*, 793.
- (25) Schmidt, R. D.; Shultz, D. A.; Martin, J. D. *Inorg. Chem.* **2010**, *49*, 3162.
- (26) Schmidt, R. D.; Shultz, D. A.; Martin, J. D.; Boyle, P. D. *J. Am. Chem. Soc.* **2010**, *132*, 6261.
- (27) Blackman, A. *Eur. J. Inorg. Chem.* **2008**, 2633.
- (28) Beni, A.; Dei, A.; Laschi, S.; Rizzitano, M.; Sorace, L. *Chem.—Eur. J.* **2008**, *14*, 1804.
- (29) Simmons, H. E.; Fukunaga, T. *J. Am. Chem. Soc.* **1967**, *89*, 5208.
- (30) Frank, N. L.; Clérac, R.; Sutter, J. –P.; Daro, N.; Kahn, O.; Coulon, C.; Green, M. T.; Golhen, S.; Ouahab, L. *J. Am. Chem. Soc.* **2000**, *122*, 2053.
- (31) Dürr, H.; Gleiter, R. *Angew. Chem., Int. Ed. Engl.* **1978**, *17*, 559.
- (32) Dei, A.; Sorace, L. *Dalton Trans.* **2003**, 3382.
- (33) Affronte, M.; Beni, A.; Dei, A.; Sorace, L. *Dalton Trans.* **2007**, 5253.
- (34) Duhme, A. –K.; Davies, S. C.; Hughes, D. L. *Inorg. Chem.* **1998**, *37*, 5380.
- (35) Abrahams, B. F.; Price, D. J.; Robson, R. *Angew. Chem.* **2006**, *45*, 806.
- (36) Abrahams, B. F.; Boughton, B. A.; Choy, H.; Clarke, O.; Grannas, M. J.; Price, D. J.; Robson, R. *Inorg. Chem.* **2008**, *47*, 9797.
- (37) Alley, K. G.; Poneti, G.; Aitken, J. B.; Hocking, R. K.; Moubaraki, B.; Murray, K. S.; Abrahams, B. F.; Harris, H. H.; Sorace, L.; Boskovic, C. *Inorg. Chem.* **2012**, *51*, 3944.
- (38) (a) Carugo, O.; Djinovic, K.; Rizzi, M.; Bisi Castellano, C. *J. Chem. Soc., Dalton Trans.* **1991**, 1551. (b) Mulyana, Y.; Nafady, A.; Mukherjee, A.; Bircher, R.; Moubaraki, B.; Murray, K. S.; Bond, A. M.; Abrahams, B. F.; Boskovic, C. *Inorg. Chem.* **2009**, *48*, 7765.
- (39) Touceda Tourón, P.; Mosquera Vázquez, S.; Lima, M.; Lapini, A.; Fohhi, P.; Dei, A.; Righini, R. *Phys. Chem. Chem. Phys.* **2012**, *14*, 1038.
- (40) Benelli, C.; Dei, A.; Gatteschi, D.; Pardi, L. *Inorg. Chim. Acta* **1989**, *163*, 99.
- (41) Caneschi, A.; Dei, A.; Gatteschi, D.; Tangoulis, V. *Inorg. Chem.* **2002**, *41*, 3508.
- (42) Wheeler, D. E.; McCusker, J. K. *Inorg. Chem.* **1998**, *37*, 2296.

- (43) Clérac, R.; Cotton, F. A.; Dunbar, K. R.; Lu, T.; Murillo, C. A.; Wang, X. *J. Am. Chem. Soc.* **2000**, *122*, 2272.
- (44) Shultz, D. A. *Magnetism – From Molecules to Materials* Miller, J.S., Drillon, M., Eds.; Wiley, VCH: Weinheim, 2001.
- (45) Adams, D. M.; Hendrickson, D. N. *J. Am. Chem. Soc.* **1996**, *118*, 11515.
- (46) Jung, O. -S.; Pierpont, C. G. *Inorg. Chem.* **1994**, *33*, 2227.
- (47) Caneschi, A.; Cornia, A.; Dei, A. *Inorg. Chem.* **1998**, *37*, 3419.
- (48) Dei, A.; Feis, A.; Poneti, G.; Sorace, L. *Inorg. Chim. Acta* **2008**, *361*, 3842.
- (49) Telfer, S. G.; Bocquet, B.; Williams, A. F. *Inorg. Chem.* **2001**, *40*, 4818.
- (50) Nagao, H.; Komeda, N.; Mukaida, M.; Suzuki, M.; Tanaka, K. *Inorg. Chem.* **1996**, *35*, 6809.
- (51) D'Alessandro, D.; Keene, F. R. *Chem. Soc. Rev.* **2006**, *35*, 424.
- (52) Bencini, A.; Beni, A.; Costantino, F.; Dei, A.; Gatteschi, D.; Sorace, L. *Dalton Trans.* **2006**, 722.
- (53) Juhász, G.; Matsuda, R.; Kanegawa, S.; Inoue, K.; Sato, O.; Yoshizawa, K. *J. Am. Chem. Soc.* **2009**, *131*, 4560.
- (54) Graf, M.; Wolmershäuser, G.; Kelm, H.; Demeschko, S.; Meyer, F.; Krüger, H. -J. *Angew. Chem., Int. Ed.* **2010**, *49*, 950.
- (55) Roux, C.; Adams, D. M.; Itie, J. P.; Polian, A.; Hendrickson, D. N.; Verdagner, M. *Inorg. Chem.* **1996**, *35*, 2846.
- (56) Yokoyama, T.; Okamoto, K.; Nagai, K.; Ohta, T.; Hayami, S.; Gu, Z. -Z.; Nakajima, R.; Sato, O. *Chem. Phys. Lett.* **2001**, *345*, 272.
- (57) Poneti, G.; Mannini, M.; Sorace, L.; Sainctavit, P.; Arrio, M. -A.; Rogalev, A.; Wilhelm, F.; Dei, A. *ChemPhysChem* **2009**, *10*, 2090.
- (58) Hudson, A.; Luckhurst, G. R. *Chem. Rev.* **1969**, *69*, 191.
- (59) Freed, J. H.; Fraenkel, G. K. *J. Chem. Phys.* **1962**, *37*, 1156.
- (60) Bolton, J. R.; Carrington, A. *Mol. Phys.* **1962**, *5*, 161.
- (61) Collison, D.; Mabbs, F. E.; Turner, S. S. *J. Chem. Soc. Farad. Trans.* **1993**, *89*, 3705.
- (62) Elschenbroich, C.; Wünsch, M.; Behrend, A.; Metz, B.; Neumüller, B.; Harms, K. *Organometallics* **2005**, *24*, 5509.
- (63) Freed, J. H.; Fraenkel, G. K. *J. Chem. Phys.* **1963**, *39*, 326.
- (64) Jacobsen, C. J. H.; Pedersen, E.; Villadsen, J.; Weihe, H. *Inorg. Chem.* **1993**, *32*, 1216.
- (65) Shultz, D. A.; Boal, A. K.; Farmer, G. T. *J. Org. Chem.* **1998**, *63*, 9462.
- (66) Shultz, D. A.; Mussari, C. P.; Ramanathan, K. K.; Kampf, J. W. *Inorg. Chem.* **2006**, *45*, 5752.
- (67) Simmons, H. E.; Fukunaga, T. *J. Am. Chem. Soc.* **1967**, *89*, 5208.
- (68) Britovsek, G. J. P.; England, J.; White, A. J. P. *Inorg. Chem.* **2005**, *44*, 8125.